Incorporating Network Scale River Bathymetry to Improve Characterization of Fluvial Processes in Flood Modeling

Sayan Dey[1], Siddharth Saksena[2], Danielle Winter[3], Venkatesh Merwade[1], Sara McMillan[3]

[1]Lyles School of Civil Engineering, Purdue University, West Lafayette, IN, USA.

[2]Via Department of Civil and Environmental Engineering, Virginia Polytechnic Institute and State University, Blacksburg, VA, USA.

[3]Department of Agricultural and Biological Engineering, Purdue University, West Lafayette, IN, USA.

Corresponding author: Sayan Dey (dey6@purdue.edu)

Key Points:

- The effect of river geometry on subsurface processes, such as infiltration and lateral seepage in large-scale fluvial modeling is highlighted
- Subsurface processes in the floodplain are controlled by overall channel characteristics, rather than channel shape
- Channel conveyance capacity and longitudinal slope are critical bathymetric controls of subsurface processes in floodplains of river network

Abstract

Several studies have focused on the importance of river bathymetry (channel geometry) in hydrodynamic routing along individual reaches. However, its effect on other watershed processes such as infiltration and surface water (SW) – groundwater (GW) interactions has not been explored across large river networks. Surface and subsurface processes are interdependent, therefore, errors due to inaccurate representation of one watershed process can cascade across other hydraulic or hydrologic processes. This study hypothesizes that accurate bathymetric representation is not only essential for simulating channel hydrodynamics but also affects subsurface processes by impacting SW-GW interactions. Moreover, quantifying the effect of bathymetry on surface and subsurface hydrological processes across a river network can facilitate an improved understanding of how bathymetric characteristics affect these processes across large spatial domains. The study tests this hypothesis by developing physically-based distributed models capable of bidirectional coupling (SW-GW) with four configurations with progressively reduced levels of bathymetric representation. A comparison of hydrologic and hydrodynamic outputs shows that changes in channel geometry across the four configurations has a considerable effect on infiltration, lateral seepage, and location of water table across the entire river network. In addition, the results from this study provide insights into the level of bathymetric detail required for accurately simulating flooding-related physical processes while also highlighting potential issues with ignoring bathymetry across lower order streams such as spurious backwater flow, inaccurate water table elevations, and incorrect inundation extents.

1 Introduction

River bathymetry is critical for simulating fluvial hydrodynamics accurately in flood inundation mapping. Several studies have investigated the impact of poor bathymetric representation on one- and two-dimensional flow models and concluded that river bathymetry affects hydraulic attributes significantly. Specifically, inaccurate estimation of channel storage capacity may lead to errors in predicting the depth and extent of inundation. Similarly, errors in estimating longitudinal slope affect the magnitude of streamflow and erroneous thalweg representation can contribute to poor estimation of shear and velocity (Cook and Merwade, 2009; Dey, 2016; Dey et al., 2019; Grimaldi et al., 2018; Saleh et al., 2012). However, these studies have only focused on the influence of river bathymetry on hydrodynamic simulations, usually along a single reach, and not the entire river network. The hydrodynamic models implemented by these studies ignore within reach hydrologic processes and route the flood wave along the river channel using known surface boundary conditions such as flow or stage hydrographs derived from gauges or estimated from loosely coupled hydrologic model.

Fluvial systems involve a complex interplay between various hydrologic and hydraulic processes such as rainfall-generated surface runoff, infiltration and surface water – groundwater (SW-GW) interactions, in addition to hydrodynamic flow regimes along river channels. (Fleckenstein et al., 2010; Kollet and Maxwell, 2008; Saksena and Merwade, 2017a; Stewart et al., 1999). Several studies have shown that stream-aquifer interactions are sensitive to WSE fluctuations in the river (Flipo et al., 2014; Tran et al., 2020; Vergnes and Habets, 2018). The water table (GWT) at the floodplains is highly correlated with the WSE in the river (Claxton et al., 2003; Jung et al., 2004). Coupled with the fact that river geometry is one of the most important factors affecting WSE, errors in WSE estimation can propagate to these hydrologic processes. Therefore,

the inadequate topographic representation that results from excluding river bathymetry can influence how surface and subsurface processes interact with each other in a simulation model (Cardenas and Jiang, 2010; Wörman et al., 2006). The cascading effects of inaccurate bathymetric representation are obscured to some degree in loosely coupled hydrologic and hydrodynamic (H&H) models traditionally implemented in large-scale flood modeling applications because the upstream boundary conditions and lateral inflows for simulating river hydrodynamics are estimated separately using hydrologic models with simplistic surface routing (Baratelli et al., 2016; Follum et al., 2020; Rajib et al., 2020; Saleh et al., 2012; Vergnes and Habets, 2018). Loose coupling enables hydrologic fluxes such as discharge to move from land surface to river but ignores potential feedbacks such as backwater effects and hyporheic exchanges which might be exacerbated by the lack of river bathymetry, especially at large watershed scales (Brunner et al., 2017; Käser et al., 2014; Mejia and Reed, 2011).

There is an increasing interest in developing high-resolution flood models spanning regional or continental scales, owing to considerable advances in H&H model capabilities and data acquisition techniques (Altenau et al., 2017; Grimaldi et al., 2019; Käser et al., 2014; Saksena et al., 2019; Tijerina et al., 2021). However, river bathymetry information, which is essential for accurate flood modeling, is not available for river networks across large spatial domains. Field surveys for acquiring bathymetry are impractical for river networks spanning hundreds of kilometers, while remote sensing techniques such as bathymetric Lidar and photogrammetry are limited to shallow and clear river reaches only (Feurer et al., 2008; Gao, 2009; Legleiter et al., 2015; Pan et al., 2015). A useful alternative for large-scale river bathymetry estimation is the application of conceptual models that can estimate bathymetry based on easily accessible data using functional surfaces. Several studies have implemented different bathymetric shapes ranging

from simplistic symmetric shapes such as rectangles, triangles and parabolas (Czuba et al., 2019; Grimaldi et al., 2018; Trigg et al., 2009) to more complex functional surfaces based on hydraulic and geomorphologic concepts (e.g., Bhuyian et al., 2015; Brown et al., 2014; Merwade, 2004; Price, 2009). These conceptual models try to estimate shapes that reflect certain bathymetric characteristics of the actual riverbed (such as longitudinal slope, thalweg elevation) while ignoring other bathymetric characteristics as is the case for channel side-slope (bank slope) when rectangular channels are implemented. The underlying assumption for implementing these conceptual bathymetric models as an alternative to detailed bathymetric surveys in H&H models is that they contain just enough bathymetric detail to produce acceptable H&H simulations. Such an assumption requires a comprehensive understanding of the effect of bathymetric representation on flooding related physical processes to ensure that essential bathymetric characteristics are accurately incorporated.

Several studies have analyzed the effect of bathymetry on channel hydrodynamics (Dey et al., 2019; Grimaldi et al., 2018; Saleh et al., 2012; Trigg et al., 2009), but they have ignored the effect of bathymetry on subsurface hydrological processes, especially for tightly coupled H&H models spanning large spatial domains. Prior works exploring the impact of river bathymetry on surface-subsurface interactions have been conducted on relatively small spatial scales such as across a meander or along a single reach. For example, Chow et al. (2018) used field measurements to show that appropriate representation of asymmetry in channel geometry is critical for accurate estimation of hyporheic exchanges at a river meander. Doble et al., (2012) demonstrated that the surface-subsurface interactions in the vicinity of the river are affected by the side-slope of river channels (riverbank slope) for a field-scale study. Similarly, Mejia and Reed (2011) demonstrated the importance of bathymetry in single reaches by implementing a loosely coupled hydrologic and

hydraulic modeling framework. These studies have shown that river bathymetry impacts the surface-subsurface hydrodynamics at the reach scale. Hydrologic and hydrodynamic processes aggregate and interact differently as we move from single reach to large river networks spanning an entire watershed (Saksena et al., 2021). Therefore, there is a need to evaluate the influence of river bathymetry on hydrologic processes across large river networks. Addressing this need is critical for enabling effective and parsimonious incorporation of river bathymetry in regional or continental scale models for flood simulations.

Considering the above discussion, the overarching aim of this study is to provide a comprehensive understanding of the impact of river bathymetry on flooding-related surface and subsurface processes at a river network scale. Prior studies investigating this topic have either focused on river bathymetry's effect on channel routing only, thereby ignoring the interdependence between surface and subsurface processes including SW-GW interactions or explored its effect on within reach subsurface hydrological processes at small spatial scales (reach scale or smaller). This study overcomes the limitations of prior studies by creating large-scale physically-based distributed models to demonstrate that the effect of river bathymetry on not just fluvial channel routing, but also SW – GW interactions and infiltration. Past studies have shown how the lack or inclusion of river bathymetry impacts the flood inundation estimation, but this study aims to shed light on its effect on the physical process affecting flood simulation across a river network thereby facilitating efficient bathymetry incorporation for accurately simulating large-scale flooding-related surface and subsurface processes in data-sparse regions. Specifically, the objectives of this study are to: (i) quantify the effect of river bathymetry incorporation on surface and subsurface physical processes, including their interactions, across large river networks; and (ii) identify specific bathymetric characteristics, such as channel conveyance, channel asymmetry and channel

thalweg, that control surface and subsurface physical processes in floodplains. These objectives are accomplished by simulating the hydrology and hydrodynamics of two watersheds and analyzing the fluxes for four different levels of bathymetric details across the river network.

2 Study Area and Data

The objectives presented in Introduction can be accomplished by using watersheds that are expected to produce significantly different SW-GW interactions. Accordingly, we selected two study areas in Indiana, presented in Figure 1(a) and Table 1, with distinct geomorphic, soil and land use characteristics, but similar climatological and geologic characteristics. The first study area is a portion of the Upper Wabash River Basin (referred to as the UWR) with an area of 1,757 km^2. This study area contains the Wabash River, extending from the city of Logansport to Lafayette, and three major tributaries: Tippecanoe River, Wildcat Creek, and Deer Creek. These four streams vary in length, average width, and depth (Table 1). Additionally, Tippecanoe River and Wildcat Creek are highly sinuous compared to Wabash River and Deer Creek. This region has experienced several extreme events in 2005, 2008, 2013 and 2018, causing widespread flooding. The geology of the region consists of glacial till deposits, fertile soils, and shallow aquifers, with a deep confining layer of shale (Saksena and Merwade, 2017b). While there are some developed regions around Lafayette and Logansport, the area is primarily agricultural with high percentage of forest and agricultural land use in the floodplains as presented in Table 1.

The second study area, with an area of 370 km^2, is a part of the White River Basin (referred to as WHR), encompassing the City of Indianapolis and contains three major tributaries: Fall Creek, Williams Creek, and Crooked Creek. The streams in this area have smaller variability in geomorphologic characteristics (Table 1) compared to UWR. For example, the White River, Williams Creek and Crooked Creek all have similar sinuosities. Because this region is highly

153 urbanized, there are several drop structures, artificial lakes, and detention ponds in the floodplain
154 of the White River. Additionally, the developed regions in the floodplain of White River are
155 protected by levees.

156 Topography, surface roughness (Manning's *n*), and upstream boundary conditions are the
157 primary inputs to hydrodynamic models, and so we obtained high-quality Lidar-based DEMs for
158 both study areas from the Indiana Spatial Data Portal (ISDP). Additionally, bathymetric survey
159 data are available for 26 cross-sections near the Tippecanoe-Wabash confluence (Figure 2). The
160 DEM resolution for UWR and WHR is 9 m and 3 m, respectively. A relatively coarser DEM is
161 used for UWR to address the computational constraints due to its size, which is approximately 5
162 times larger compared to WHR. The analysis presented here primarily focuses on comparison of
163 differences in hydrologic and hydrodynamic fluxes due to differences in bathymetric
164 configurations in the same watershed. The DEM resolution used for creating different models
165 belonging to a specific watershed remains unchanged to ensure consistency in comparing results
166 from models with different bathymetric configurations. Additionally, the DEM resolutions for both
167 watersheds are within the hyper-resolution range (< 10m) for flood models and are not expected
168 to affect the results.
169

170 **Table 1.** Study area description

Geomorphological Characteristics					
		UWR			
Name	*Length (km)*	*Average Width (m)*	*Average Depth (m)*	*Slope* $(\times 10^{-3})$	*Sinuosity*
Wabash River	83.01	136.0	1.74	0.3	1.22
Tippecanoe River	30.76	84.2	1.52	0.5	1.93
Wildcat Creek	8.59	54.6	0.70	0.7	2.06
Deer Creek	8.03	34.6	0.76	1.2	1.28
		WHR			
Name	*Length (km)*	*Average Width (m)*	*Average Depth (m)*	*Slope* $(\times 10^{-3})$	*Sinuosity*
White River	42.8	83.2	1.58	0.4	1.48
Fall Creek	14.8	40.9	0.86	1.0	1.26
Williams Creek	7.3	13.3	1.43	3.1	1.48
Crooked Creek	2.5	15.6	1.45	2.3	1.49

Landuse as per NLCD 2011 (%)				
Type	*UWR*		*WHR*	
	Study Area	*Floodplain*	*Study Area*	*Floodplain*
Agricultural	77	50	3	4
Forest	12	27	4	7
Water	2	9	3	9
Urban/Developed	10	14	89	81

Soil Group as per NRCS gSSURGO (%)		
Soil Type	*UWR*	*WHR*
A	13.8	0.1
B	56.2	51.5
C	29.8	48.3
D	0.2	0.1

171

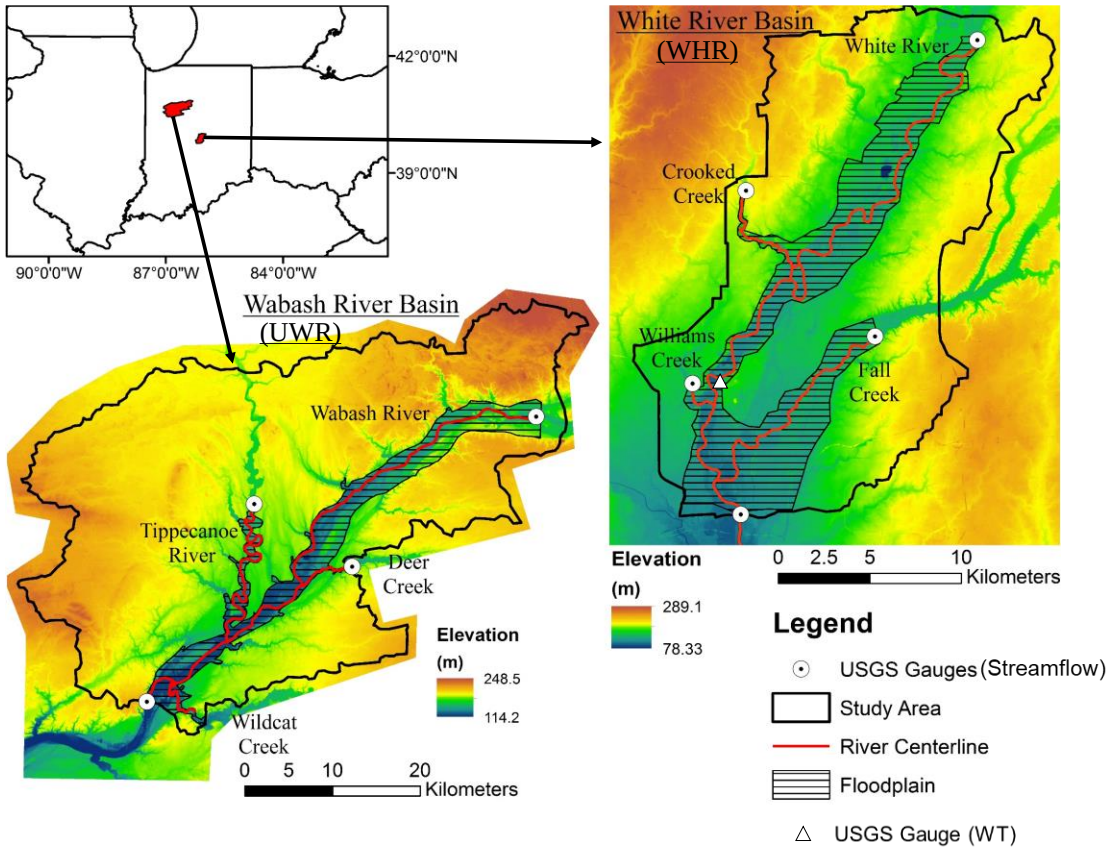

(a)

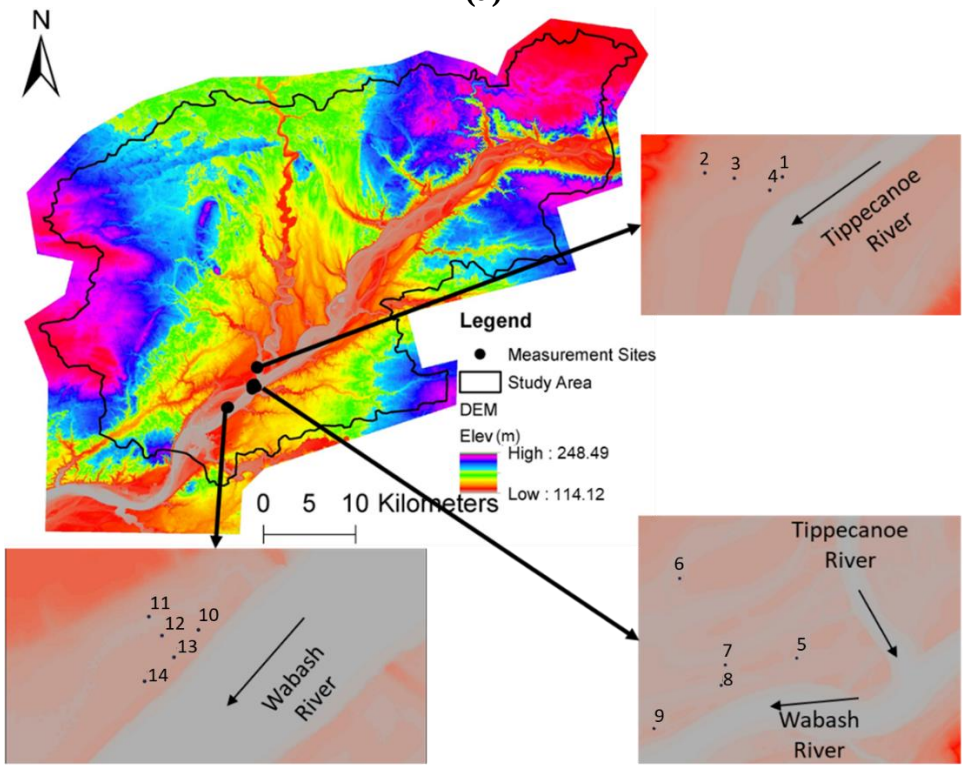

(b)

Figure 1. (a) Location map of the study areas and (b) field survey sites for GWT at UWR

177 The distributed hydrologic modeling approach used in this study requires data related to
178 land use, streamflow, rainfall, soil properties and aquifer characteristics. The land use data are
179 obtained from the National Land Cover Database (NLCD) from the Natural Resources
180 Conservation Service (NRCS). The roughness values (Manning's *n*) for the different land use
181 classes in the study areas are obtained from Saksena and Merwade (2015). The upstream boundary
182 condition for each stream is determined by incorporating streamflow hydrographs obtained from
183 United States Geologic Survey (USGS) gages, which also provide river depth information at those
184 locations. The rainfall data are obtained from the North American Land Data Assimilation System
185 (NLDAS) at a 12-km grid resolution. The soil types are characterized using the Hydrologic Soil
186 Group (HSG) classification provided in NRCS's Gridded Soil Survey Geographic database
187 (gSSURGO).

188 The outlet of UWR (shown in Figure 1(a)) is located at the USGS gage 03335500 Wabash
189 River at Lafayette, IN, and the outlet for the WHR is located at the USGS gage 03353000, White
190 River at Indianapolis, IN. These outlet gages are used for validating the physically-based
191 distributed models used in this study. Additionally, the GW component of the models is validated
192 using within-reach observations of water table at specific locations. In WHR, there is a USGS
193 gauge (USGS 394952086110901) which monitors GWT elevation near the White River (Figure
194 1(a)). However, there is no such continuous GWT monitoring station in UWR. Therefore, site
195 visits were organized for measuring water table depths at multiple locations in the Wabash River
196 floodplain and near the Wabash River – Tippecanoe River confluence (Figure 1(b)). The water
197 table was measured by using 2m deep piezometers in two different seasons: Winter 2018 (16th
198 Dec 2018) across 8 locations (Points 1, 4, 5, 8 – 10, 13, and 14) and Summer 2019 (24th July 2019)
199 across 9 locations (Points 2 – 4, 6 – 8 and 11 – 13).

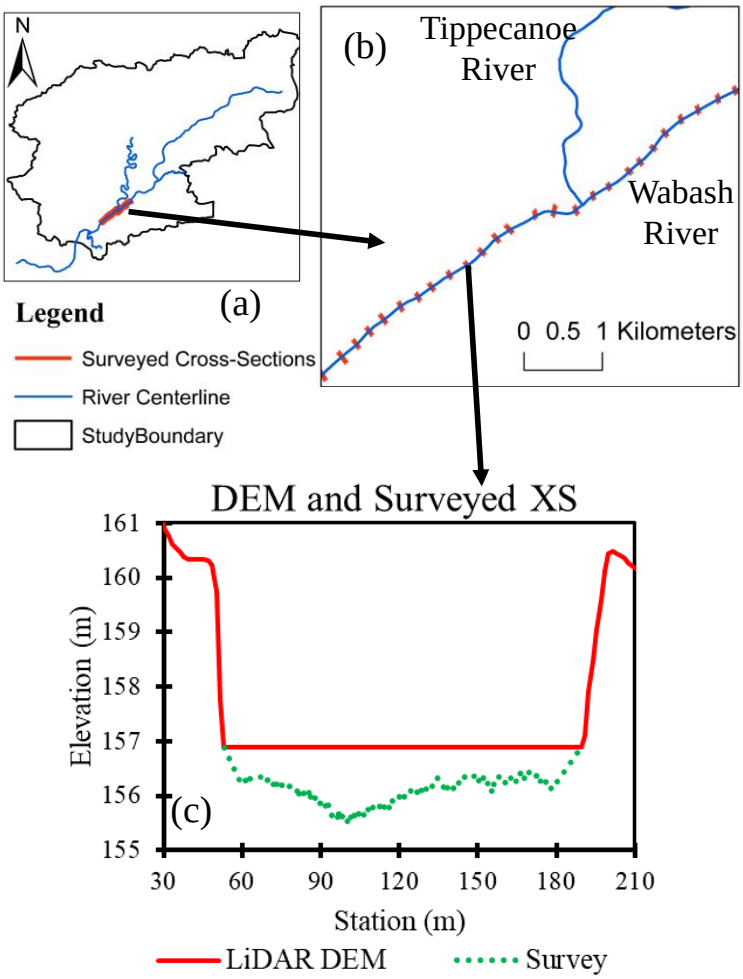

Figure 2: Figure showing (a) the location of surveyed cross-sections in UWR, (b) close-up of the surveyed cross-sections, and (c) comparison of one of the surveyed cross-section and LiDAR DEM derived cross-section at that location

3 Experimental Design

A major constraint in quantifying the impact of river bathymetry impact on watershed processes is the absence of bathymetric data for river networks across large spatial domains. In this study, first a conceptual bathymetric model (described in Section 4) calibrated with surveyed bathymetric data is implemented to create a bathymetric representation comprising of asymmetric cross-sections with realistic side slopes (bank slopes). This configuration, with the best 3D river network among all configurations, is designated as Control.

Next, two more bathymetric configurations are created by reducing the level of detail incorporated in the 3D river network. One configuration (M1) has a rectangular cross-section that preserves both the area (channel storage) and the depth (thalweg elevation) of cross-sections as compared to Control but ignores the side slope and the asymmetry in river cross-sections. It should be noted that information about channel conveyance capacity (bankfull area) is not readily available for river networks. However, some studies have developed alternative methods to estimate the channel conveyance capacity, including drainage area-based regionalization equations as well as the algorithms developed for the upcoming Surface Water and Ocean Topography (SWOT) mission(Rodríguez et al., 2020; Schaperow et al., 2019; Yoon et al., 2012). This configuration can provide insights into the suitability of such parsimonious methods for incorporating bathymetry as well as the role of channel asymmetry and side slope on subsurface hydrological processes in large-scale river networks.

The next configuration (M2) also has a rectangular cross-section but only preserves the depth (thalweg elevation) of cross-sections but not the area (channel storage). This configuration has previously been deployed in studies where sufficient bathymetry data is not available from boat surveys that only capture the longitudinal channel profile (example: Czuba et al., (2019); Grimaldi et al., (2018)). Finally, the Lidar derived DEM without any bathymetry incorporation (M3) is also created. The inclusion of M3 can show what processes are significantly impacted (or not impacted) by the incorporation of river bathymetry and highlight a potential error source for H&H models in data sparse regions. This configuration is expected to perform poorly as compared to the other three configurations. This configuration is included for contextualizing the results of M1 and M2 with respect to “Control”.

These four configurations (Control, M1, M2 and M3) are simulated using a tightly coupled physically-based distributed model (described in Section 5) capable of capturing the complex interplay of various hydrologic and hydrodynamic processes that govern the movement of water in a watershed. The hydrologic and hydrodynamic outputs of M1, M2 and M3 are compared to those estimated by "Control" to provide insights into the role of bathymetric representation on surface and subsurface processes in the floodplains of a river network.

4 Bathymetric Model Development

Previous studies have implemented a wide range of functional surfaces as approximations for channel geometry ranging from standard geometrical shapes, such as parabola, rectangle or exponential curve (Czuba et al., 2019; Grimaldi et al., 2018; Trigg et al., 2009) to more intricate channel representations based on geomorphological concepts (e.g., Bhuyian et al., 2015; Brown et al., 2014; Merwade, 2004; Price, 2009). These conceptual models are designed for estimating bathymetry for a single reach only, which is usually the main stem of a river network. This study implements a network-scale river bathymetry generation called the System for Producing RIver Network Geometry (SPRING). Some features of this model have been adapted from Merwade (2004).

SPRING first creates bathymetry for each individual reach (Step-1) following the procedure of Merwade (2004), and then these reach-scaled bathymetry datasets are joined by creating bathymetry at river confluences (Phase-2). The end result from SPRING is a 3D representation of the entire river network which can be burned into the DEM. The bathymetry generation process for each reach and confluence is briefly described below.

256 *4.1 Bathymetry generation for individual reaches*

257 To estimate the bathymetry of individual reaches, this study adapted the meandering
258 thalweg based approach of the River Channel Morphology Model (RCMM: Merwade, 2004)
259 because of its ability to account for channel anisotropy. The meandering of the thalweg is primarily
260 caused by sediment deposition on the inner bank and erosion at the outer bank of a river bend. This
261 process is conceptualized to create a set of equations (Equations 1-3) that can approximate a
262 channel cross-section (Figure 3). The inputs, in this case, are channel centerline, banks, DEM, and
263 depth of the river at multiple locations along the channel network. The methodology, adopted from
264 Merwade (2004) and Dey et al., (2019), is described briefly in *Appendix A1*.

265 $$t^* = \begin{cases} a(r^*)^{-b} - 0.5, & r^* \leq 2 \\ 0, & r^* > 2 \end{cases} \quad \text{(Equation 1)}$$

266 $$z^*(n^*) = \{f(n^*|\alpha_1, \beta_1) + f(n^*|\alpha_2, \beta_2)\} \times k \quad \text{(Equation 2)}$$

267 $$z(n^* \times W) = z_{bank} - z^*(n^*) \times depth \quad \text{(Equation 3)}$$

268 where, $r^*$is the normalized radius of curvature of a river segment ($r^* = r/w$), t^* is the
269 normalized thalweg location at a cross-section ($t^* = t/w$), w is the average width of the river
270 segment, a and b are constants, z^* is the normalized depth of the channel bed at a distance n^*
271 along the cross-section from the center of the channel, $f(n^*|\alpha_1, \beta_1)$ is the beta probability
272 distribution function (pdf) with parameters $\alpha_1$and β_1, $f(n^*|\alpha_2, \beta_2)$ is the beta pdf with parameters
273 α_2 and β_2 and k is a scaling parameter. Using a linear combination of two beta pdfs enables
274 SPRING to model asymmetric cross-section shapes by varying its parameters. The parameters of
275 SPRING ($a, b, \alpha_1, \alpha_2, \beta_1, \beta_2$) are calibrated using surveyed cross-sections using the Particle Swarm
276 Optimization technique.

277

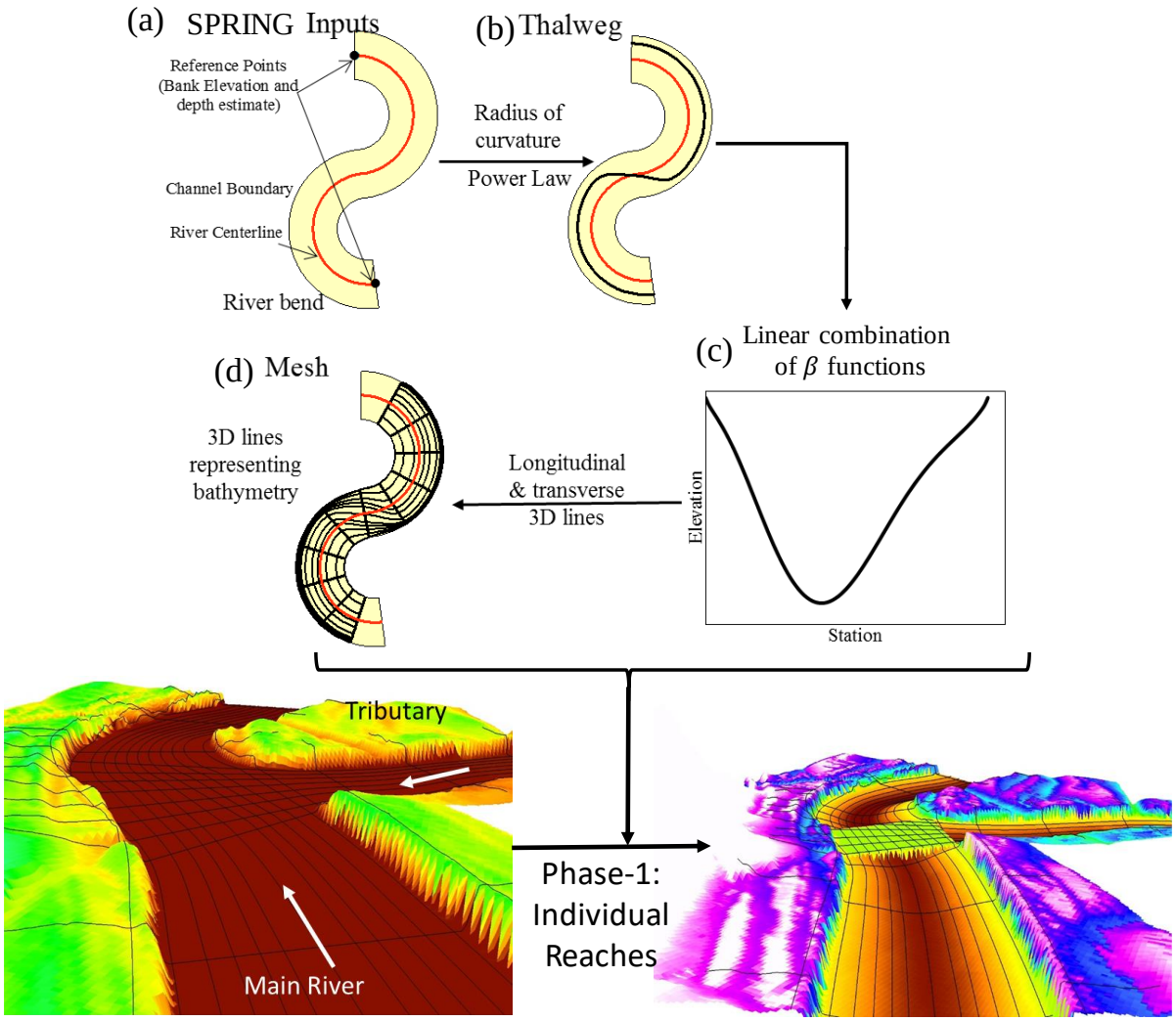

278

279 **Figure 3.** Workflow of SPRING to estimate bathymetry at individual reaches. (a) The input
280 datasets; (b) estimating meandering thalweg from the radius of curvature of river centerline using
281 Equation (1); (c) Estimating asymmetric cross-sections using Equations (2) and (3); and (d)
282 creating a mesh to generate 3D representation of individual reaches. Note: Part of the figure is
283 adapted from Dey, (2016).
284

285 In the curvilinear axes adopted in this study, the lateral axis (running from left to right bank
286 perpendicular to the centerline) is positive on the right side and negative on the left side when
287 looking down the direction of flow of the river Merwade (2004). The center and radius of curvature
288 (r) are determined by the three-point arc method. If the center of curvature lies to the left of the
289 centerline, it means the river at the meander is turning to the left and the thalweg is located to the

right side of the centerline (positive t^*) and vice-versa. The elevation of the thalweg along the channel is estimated by linearly interpolating the thalweg elevation between "reference points" which are specified at locations where such information is available. Therefore, SPRING creates a piecewise linear thalweg profile with the reference points acting as points where the thalweg slope changes. Usually, reference points should be provided at the upstream and downstream ends of each reach, but SPRING can accommodate multiple references points along the same reach as well.

4.2 Bathymetry generation at confluence

Once the bathymetry for individual reaches has been estimated, the next step is to connect these individual reaches by estimating the bathymetry at the river confluences. Figure 4 depicts the methodology for estimating the confluence boundary. First, SPRING locates the confluence as the point of intersection of three or more reach centerlines. It, then, categorizes the three centerlines as "downstream mainstem", "upstream mainstem" and "tributary" channels (Figure 4(a)). This is decided based on the start and end point of the three centerlines and the drainage areas of each of the reaches draining into the confluence. The stream with the lowest drainage area is designated as a tributary. The reach downstream of the confluence is designated as the downstream mainstem. Next SPRING joins the banks of each stream to create the "confluence boundary" (Figure 4(b)). The region enclosed by the confluence boundary is used for estimating bathymetry at the confluence.

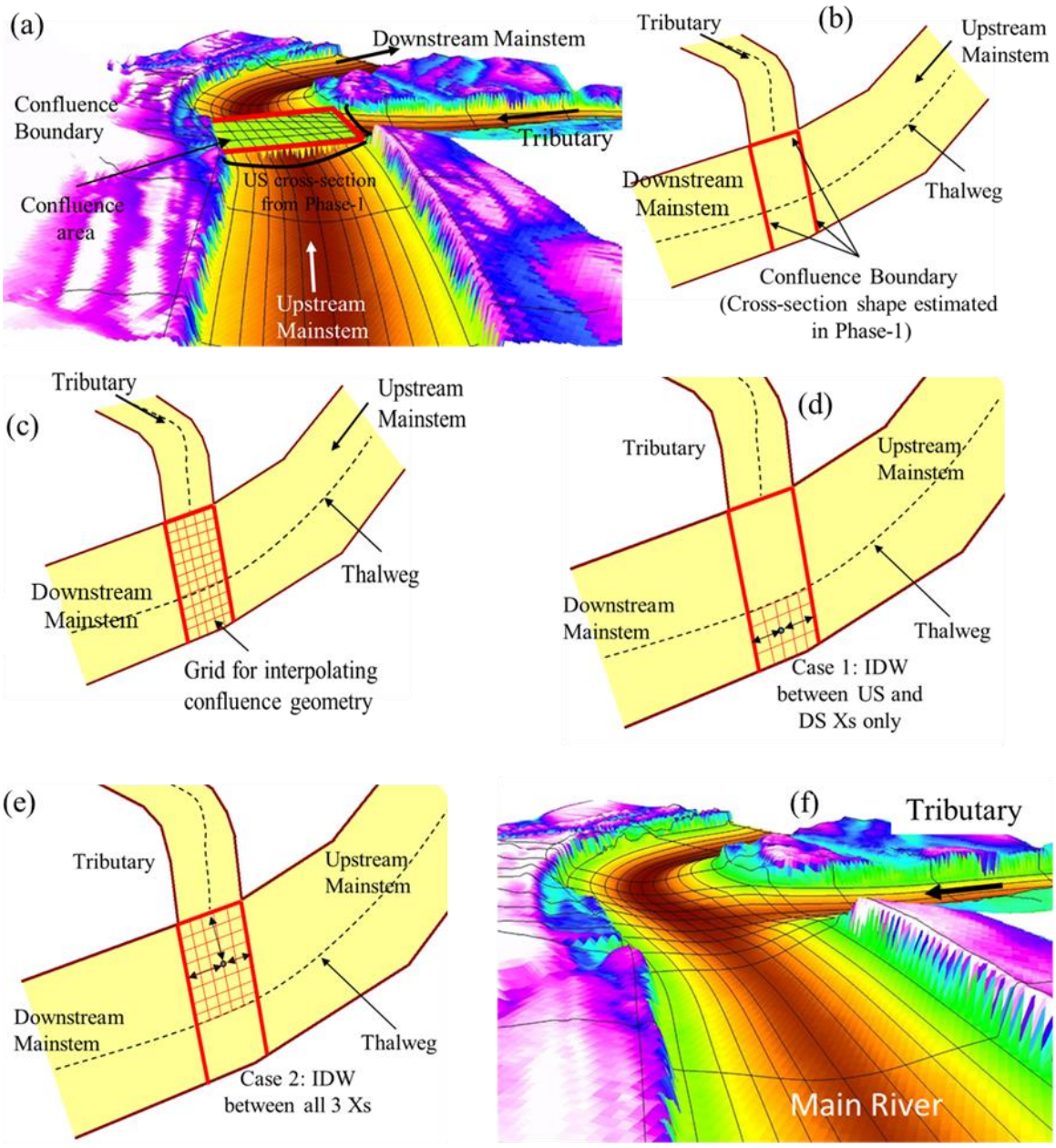

Figure 4. Figure showing the workflow for estimating channel geometry at confluences. (a) The input for Phase-2 (output of Phase-1); (b) estimating confluence boundary; (c) creating grid across confluence area; (d) interpolating geometry for Case-1 (Equation 4) for points on the other side of thalweg as the tributary; (e) interpolating geometry for Case-2 (Equation 4) for points on the same side of thalweg as the tributary, and (f) final output with hydraulically connected confluence geometry.

To estimate the bathymetry at the confluence, a variation of the inverse distance weighting (IDW) algorithm is used. SPRING creates a mesh of equidistant longitudinal lines running parallel

and transverse to the mainstem thalweg inside the confluence boundary (Figure 4(c)). For each point on the mesh, SPRING locates the closest point on each boundary cross-section. The elevations of these points on the boundary cross-sections are known from the reach bathymetry estimated in the first step (Section 3.1). The boundary cross-sections are expected to differ in geometry and maximum depth, due to the differences in drainage areas upstream and downstream of the confluence for the mainstem as well as variations in river characteristics between the tributary and the mainstem. SPRING is designed to account for these variations in the geometry of boundary cross-sections while interpolating the bathymetry at confluences.

If the mesh point is on the other side of the mainstem thalweg as compared to the tributary (Figure 4(d)), a two-point IDW is implemented between the upstream and downstream boundary cross-sections of the main stem (Case 1 in Equation 4). For mesh points lying on the same side of the mainstem thalweg as the tributary (Figure 4(e)), a three-point IDW is implemented to estimate the elevation of the mesh point as shown in Equation 4 (Case 2).

$$z = \begin{cases} \frac{z_1 d_1^{-1} + z_2 d_2^{-1}}{d_1^{-1} + d_2^{-1}}, & Case\ 1 \\ \frac{z_1 d_1^{-1} + z_2 d_2^{-1} + z_3 d_3^{-1}}{d_1^{-1} + d_2^{-1} + d_3^{-1}}, & Case\ 2 \end{cases} \quad \text{(Equation 4)}$$

where z is the elevation of the current point in confluence mesh for which elevation is being estimated, z_1, z_2 and z_3 are the elevations of the points closest to the current point on the cross-sections upstream of confluence in the main river, downstream of the confluence in the main river and in the tributary just upstream of the confluence respectively, and d_1, d_2 and d_3 are the distances of these three points from the current point. This process is repeated for all points in the confluence mesh to create a 3D representation of the confluence bathymetry.

The 3D mesh of the individual reaches and confluences together create a synthetic representation of bathymetry for the entire river network. The 3D mesh is converted to a DEM

using the Natural Neighbor interpolation technique. The final step involves burning this 3D mesh-derived raster into the raw DEM (Lidar) to generate a DEM with improved bathymetric representation.

5 Physically-based Distributed Model Description

In this study, physically-based Interconnected Channel and Pond Routing (ICPR) model (Saksena et al., 2020, 2019) that incorporates flood-related processes such as rainfall-runoff, infiltration, and SW-GW interactions in addition to surface routing is used (Figure 5). ICPR uses a flexible mesh structure to represent both the surface and the subsurface. The surface mesh comprises of 1D elements in the river channel and 2D elements elsewhere, and the subsurface is divided into three layers with each layer represented by a 2D mesh. The soil parameters governing the subsurface are tabulated in Table 2. At each timestep, the hydrology and hydraulics are simulated across each element of the surface mesh. Simultaneously, it computes the subsurface processes across the subsurface mesh and the interactions between the surface and subsurface meshes. Therefore, it can capture the interplay among surface hydrology, river hydrodynamics and subsurface processes, making it ideal for this study. For more information on ICPR and its implementation, please refer to the Appendix A-2 or the "C3" configuration in Saksena et al., (2019) or Saksena et al., (2020).

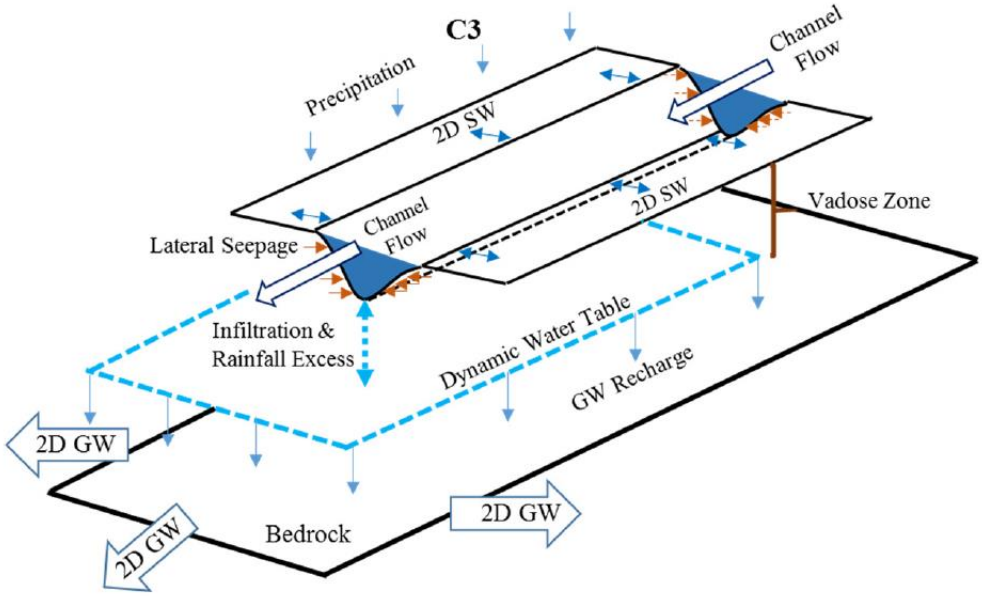

Figure 5. Conceptual illustration of physically based distributed modeling in ICPR (adapted from Saksena et al., (2019))

Table 2: Table of initial soil parameters in ICPR (adapted from Saksena et al., (2019)). K_v is vertical hydraulic conductivity, MC is the moisture content (fraction), PSI is the pore size index (dimensionless), and Ψ is the soil matric potential.

Vadose Zone	Soil Type	K_v (mm/hr)	Saturated MC	Residual MC	Initial MC	Field Capacity MC	Wilting Point MC	PSI	Ψ (cm)
Layer 1 50 cm	A	15.24	0.300	0.069	0.128	0.128	0.107	0.518	38.3
	B	6.20	0.540	0.061	0.200	0.200	0.138	0.620	25.5
	C	2.34	0.458	0.051	0.300	0.300	0.225	0.296	59.2
	D	1.40	0.620	0.053	0.240	0.240	0.118	0.161	197.9
Layer 2 50 cm	A	8.38	0.277	0.040	0.125	0.125	0.063	0.296	59.2
	B	3.10	0.280	0.070	0.170	0.170	0.135	0.316	67.5
	C	1.17	0.320	0.078	0.220	0.220	0.155	0.270	106.8
	D	0.80	0.360	0.080	0.200	0.200	0.090	0.161	197.9
Layer 3 50 cm	A	2.10	0.120	0.030	0.090	0.090	0.060	0.540	30.7
	B	0.77	0.200	0.040	0.100	0.100	0.040	0.226	99.8
	C	0.29	0.180	0.045	0.120	0.120	0.075	0.161	168.4
	D	0.20	0.190	0.045	0.090	0.090	0.060	0.161	197.9

GW Zone	Type	Effective Porosity, η_e	Hydraulic Conductivity, K (mm/hr)
Aquifer	A	0.175	30.48
	B	0.270	12.40
	C	0.310	4.67
	D	0.360	6.35

366 UWR is simulated for two continuous simulations events from 18th February 2016 to 30th
367 April 2016 (72 days) and 10th February 2018 to 15th May 2018 (94 days). WHR is simulated for
368 a one-month period from 25th May 2015 to 25th June 2015. The first 120 hours (5 days) for each
369 simulation are used as model warmup period. The model parameters have not been calibrated and
370 have been kept consistent across all four bathymetric configurations. Earlier studies using ICPR
371 (Saksena et al., 2019; Saksena and Merwade, 2017a) have shown that the model is capable of
372 producing accurate results without parameter calibration when the watershed's physical
373 description is adequately captured in the model with high-resolution input of surface and sub-
374 surface characteristics. Additionally, model calibration would alter the parameters to account for
375 any shortcomings in the simulation of hydrologic or hydraulic processes for the different
376 bathymetric configurations, thus affecting the model's behavior and rendering comparison of
377 model outputs inconsistent.

378 6 Results and Discussion

379 *6.1 Bathymetry Incorporation*

380 SPRING, described in Section 4, is implemented at both UWR and WHR to create DEMs
381 with a complete 3D representation of river network bathymetry. The channel centerline and banks
382 are digitized manually using the DEM and aerial imagery. The USGS gages provide depth of
383 channel bed at gaged locations, which are then interpolated to create channel depth at unknown
384 points along a river. The parameters of SPRING are calibrated using surveyed cross-sections.
385 Figure 6 shows the change in cross-sections and confluence bathymetry for the two basins as
386 estimated by SPRING while Figure 7 shows a comparison of the SPRING generated cross-sections
387 for Control with surveyed cross-sections.

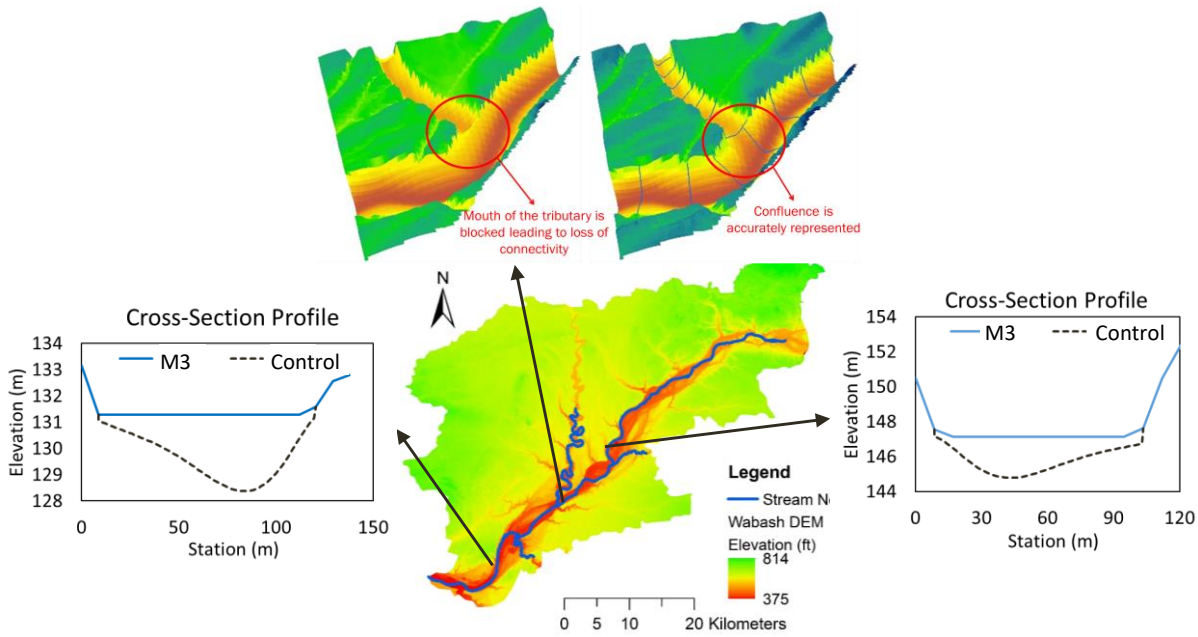

Figure 6 Examples of SPRING generated cross-sections exhibiting asymmetry in "Control" configuration and confluence topography incorporated in UWR

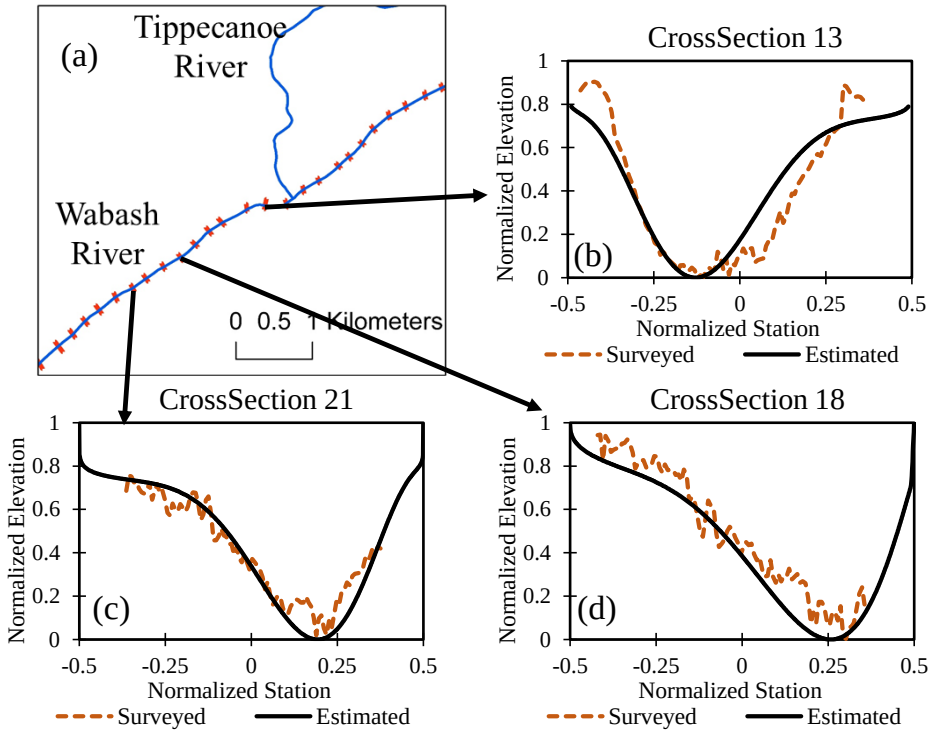

Figure 7 Comparison of surveyed and SPRING estimated cross-section shapes for "Control" at different locations along the Wabash River.

Table 3 shows the comparison of the channel characteristics, namely channel conveyance capacity (volume) and surface area of the three bathymetric configurations (M1, M2 and M3) with Control. Control and M1 have the same channel conveyance capacity but have different shapes, which leads to a difference of 0.7% in surface areas of these two networks. M1 and M2 have the same surface area but M2's channel conveyance capacity is 34.7% and 27.5% higher than Control (and M1) for UWR and WHR, respectively. The significantly larger differences in channel conveyance capacity as compared to the surface area among the bathymetric configurations is an effect of the high channel width to channel depth ratio for natural channels. Since natural river channels are much wider than they are deeper, the cross-sectional perimeter tends to be similar to the top width of the channel. Finally, M3 has the lowest surface area and channel conveyance capacity due to incomplete channel representation in the Lidar-derived DEMs.

Table 3. Percentage change in bathymetric characteristics of M1, M2 and M3 with respect to Control for the two study areas.

Study Area	Bathymetric Characteristic	Bathymetric Configuration		
		M1	M2	M3
UWR	Volume	0.0	34.7	-18.0
	Surface Area	3.1	3.1	-0.7
WHR	Volume	0.0	27.5	-27.5
	Surface Area	6.4	6.4	-0.7

Table 4 shows the change in longitudinal channel slope because of the incorporation of bathymetry. Except for Wildcat Creek in UWR, the change in slope is less than 4% for all other streams. SPRING generated channel networks have a piece-wise linear longitudinal profile with the upstream and downstream ends of the reaches having different depths due to differences in drainage areas at the two ends. Therefore, Control, M1 and M2 have identical slopes for each reach which is higher than the slopes of the reaches in M3.

417 **Table 4.** Change in longitudinal slope for each river due to bathymetry incorporation (Control,
418 M1 and M2)

River Name	Slope in Control, M1 and M2 ($\times 10^{-4}$)	Slope in M3 ($\times 10^{-4}$)	% Change
UWR			
Wabash River	3.24	3.23	0.4
Tippecanoe River	5.02	4.90	2.4
Deer Creek	12.33	11.94	3.3
Wildcat Creek	7.09	6.39	10.9
WHR			
White River	4.13	4.08	1.3
Fall Creek	9.57	9.49	0.9
Williams Creek	30.85	30.82	0.1
Crooked Creek	22.57	22.32	1.1

419

420 *6.2 Validating Control*

421 The model structure and parameters adopted in this study are validated by comparing the
422 outlet streamflow and water table elevations estimated by Control against observed data. Figure 8
423 shows the comparison of outlet hydrographs of Control for the three events and the observed
424 hydrographs from USGS gauges at those locations. The performance of Control is also quantified
425 using four performance metrics – the Nash-Sutcliffe Efficiency (NSE) (Nash and Sutcliffe, 1970),
426 Percent Bias (PBias), ratio of the root mean square error to the standard deviation of measured
427 data (RSR) and error in magnitude of highest peak flow, which are tabulated in Table 5. RSR is a
428 ratio of error in model estimate to variation in observed time-series which helps in comparing
429 RMSE across different bathymetric configurations and hydrologic outputs (timeseries). Control

exhibits high NSE and low PBias, RSR and error in peak streamflow which indicates the acceptable performance of Control for all three events across the two basins.

Table 5: Performance statistics for validating Control using USGS gauge measured streamflow at outlets and GWT timeseries

Simulation	Timeseries	NSE	PBias (%)	RSR	Error in Peak (%) *
UWR (2016)	Outlet Hydrograph	0.95	-7.2	0.23	-13.3
UWR (2018)	Outlet Hydrograph	0.96	-2.9	0.21	4.3
WHR (2015)	Outlet Hydrograph	0.95	-4.9	0.23	-8.7
WHR (2015)	GWT Elevation	0.77	-0.08	0.48	0.05

*Error in peak corresponds to the highest peak in the simulation period

The GW component of Control is validated by comparing GWT elevation estimates against GWT measurements (Figure 9). For WHR, GWT elevation timeseries observed at a USGS well is compared with the GWT estimates at that location for the 2015 simulation (Figure 9(c)) and the performance statistics are tabulated in Table 5. In the absence of USGS gauges measuring GWT in UWR, GWT is measured at 17 select locations in the floodplains of UWR by using 2m deep piezometers. Control was simulated for 21 days including the day of measurements and the GWT estimates were compared against those obtained from the piezometers. Out of these 17 datapoints, one measurement was reported as flooded (water table at the surface), and the water table was found to be deeper than 2 m (depth of piezometers) for seven cases. In all these eight cases, Control results corresponded with the observed situations. Comparison of the observed and estimated GWT elevations for the remaining nine observations where the GWT depth was within 2m is shown in Figure 9(b). RMSE for the simulated water table elevations is 0.43 m.

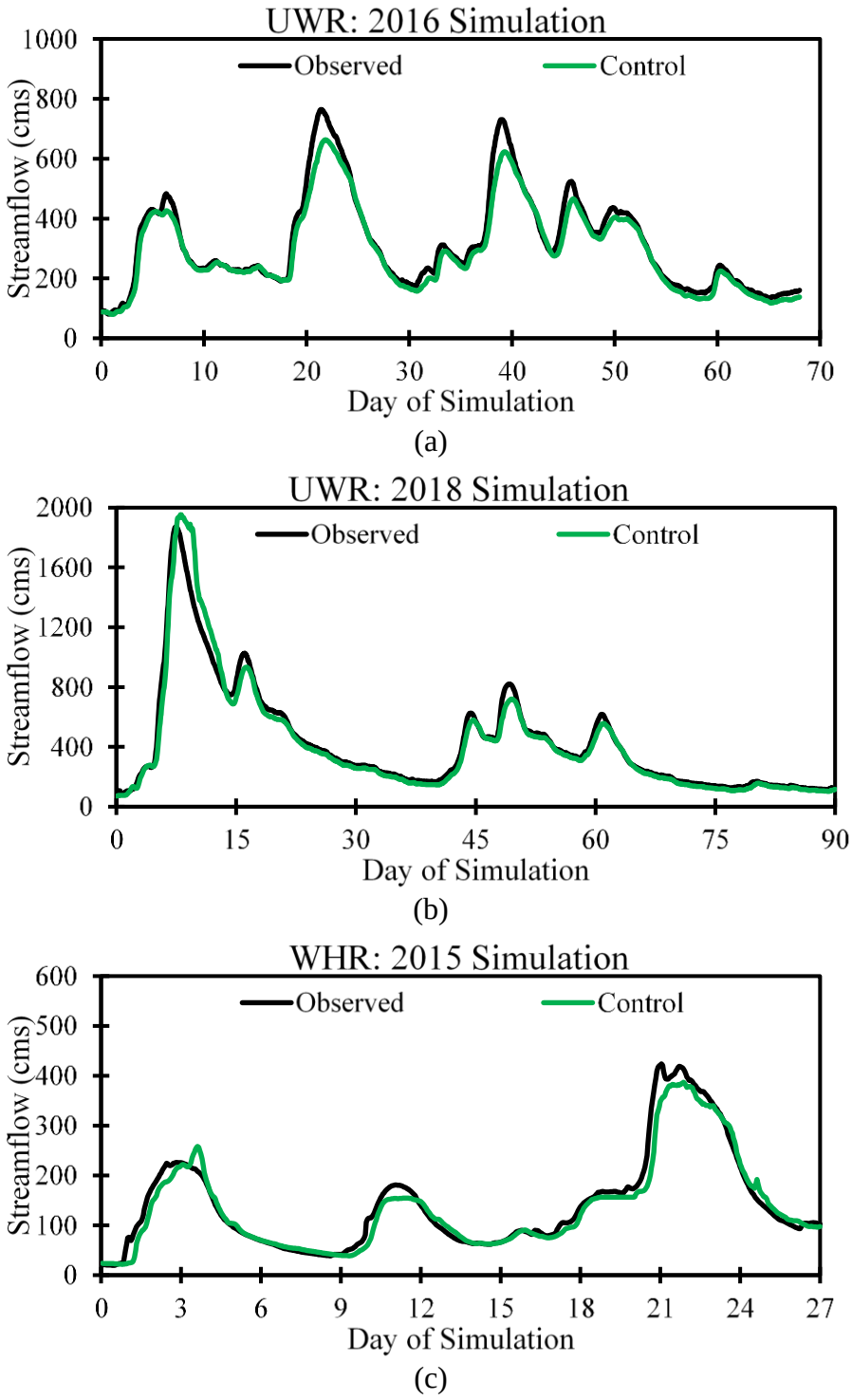

Figure 8: Comparison of outlet hydrograph of Control with observed hydrographs at the outlet of UWR for (a) 2016 simulation, (b) 2018 simulation, and (c) WHR for 2015 simulation.

The aim of the validation is not to demonstrate that the model structure and parameters are accurate; rather the validation demonstrates that the model structure and parameters reasonably characterize the surface and subsurface hydrological processes. The overall performance with respect to the water table and outlet hydrograph suggests that Control can realistically approximate the surface and subsurface hydrological processes. Additionally, the SW-GW model structure (mesh resolution) adopted in this study follows the guidelines proposed in Saksena et al (2021) for effectively capturing SW-GW interactions in tightly coupled models by considering the intrinsic scales of the surface and subsurface processes in the model structure. It should be noted that the surface and sub-surface parameters are uncalibrated and are identical across different bathymetric configurations to avoid biasing the parameters towards any particular configuration. Therefore, changing the bathymetric representation while keeping the model structure and parameters constant enables consistent comparison across different bathymetric configurations and provide insights into the role of bathymetry in simulating SW-GW interactions.

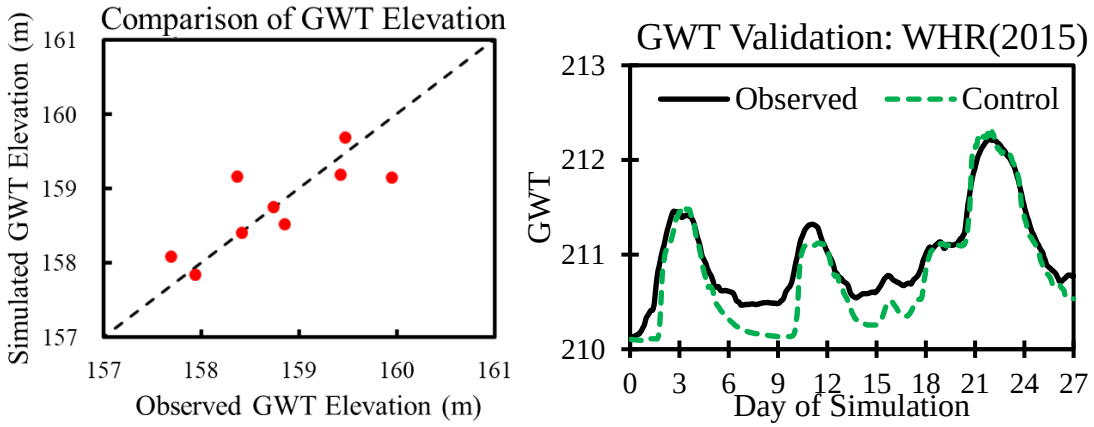

(a) (b)

Figure 9. Figure showing (a) the comparison of observed and simulated GWT for 9 locations in UWR where GWT depth is less than 2m, and (b) the comparison of observed and simulated GWT elevation timeseries for WHR at a USGS well.

473 *6.3 Effect on Overland Flow*

474 To analyze the effect of bathymetry on surface routing, the streamflow hydrographs
475 estimated at the outlets and the maximum inundation area estimated by M1, M2 and M3 are
476 compared with those estimated by Control. While streamflow at the outlet is not entirely
477 representative of the watershed response, especially for medium to large watersheds, it is a useful
478 indicator of the overall water balance across different simulations. Figure 10 shows the streamflow
479 hydrographs at the outlet for all three events corresponding to all four configurations. The relevant
480 performance metrics for quantifying the performance of M1, M2 and M3 with respect to Control
481 are tabulated in Table 6.

482 **Table 6**: Performance metrics comparing the inundation area and outlet hydrographs estimated
483 by M1, M2 and M3 with respect to Control

Simulation	Configuration	Error in Inundation Area (%)	Hydrograph Comparison at Outlet			
			NSE	PBias (%)	RSR	Error in Peak Flow (%) *
UWR (2016)	M1	-1.62	1.00	0.22	0.03	2.46
	M2	-6.84	1.00	0.24	0.05	2.58
	M3	25.36	0.81	6.19	0.44	39.76
UWR (2018)	M1	-2.78	0.97	-3.68	0.16	-10.87
	M2	-4.41	0.94	-5.56	0.24	-19.36
	M3	-0.31	0.93	0.62	0.27	-20.98
WHR (2015)	M1	1.11	0.99	1.90	0.09	6.76
	M2	-5.11	0.98	2.04	0.13	1.73
	M3	19.37	0.02	40.43	0.99	40.37

484 *Error in peak flow corresponds to the highest peak in the simulation period

485

486

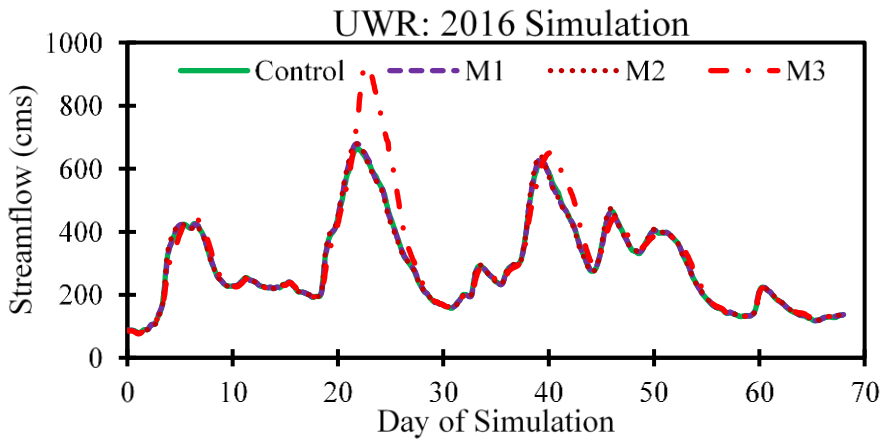

(a)

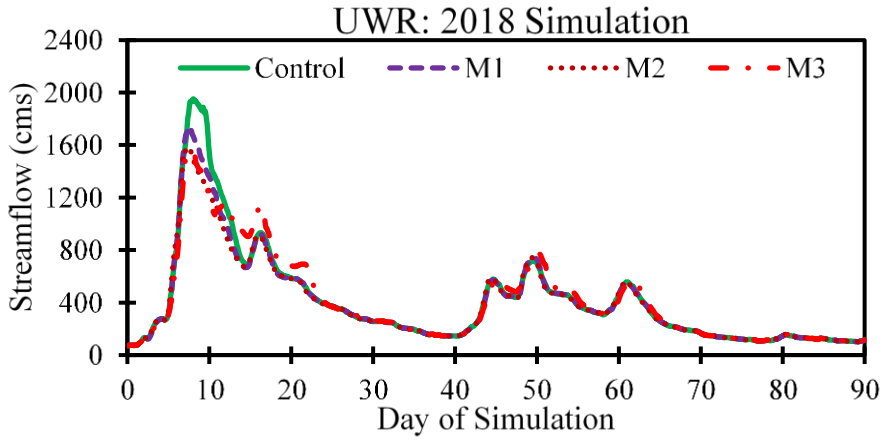

(b)

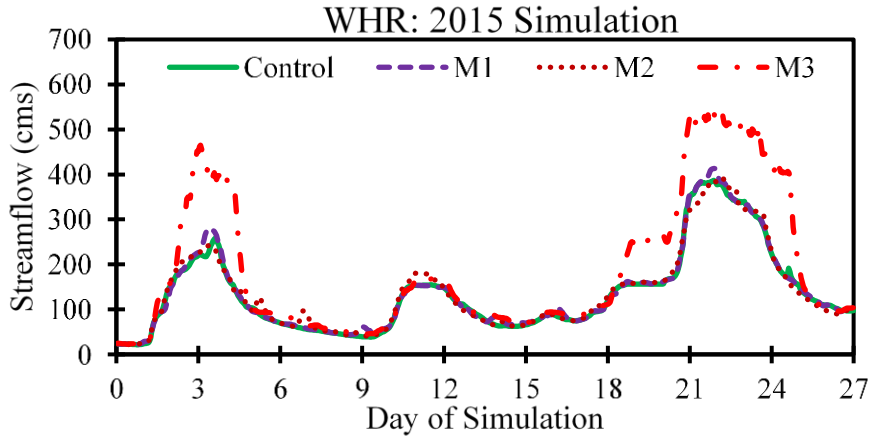

(c)

Figure 10: Comparison of outlet hydrographs of M1, M2 and M3 against Control of UWR for (a) 2016 simulation, (b) 2018 simulation and (c) WHR for 2015 simulation

491 The performance metrics (Table 6) and the outlet hydrographs (Figure 10) show that the
492 model performance depreciates with a reduction in bathymetric detail. In all cases, there is a
493 decrease in NSE and an increase in RSR and Error in Peak Flow as the bathymetric representation
494 changes from M1 to M2 and M3. The difference in performance levels is highest between M2
495 (depth information only) and M3 (no additional bathymetric detail). The addition of accurate
496 channel conveyance in addition to depth (M1 vs M2) leads to a small but not insignificant change
497 in performance, especially in terms of maximum inundation area. Finally, the difference between
498 the estimates of Control and M1 is small for both inundation area and outlet hydrographs.

499 Incorporating accurate representation of thalweg elevation for M1 and M2 (with respect to
500 Control) leads to an increase in the longitudinal slope of the river network (Table 4) as compared
501 to M3. This increase in slope increases the flow velocities in the direction of river flow for Control,
502 M1 and M2. Additionally, the channel conveyance capacity plays an important role in determining
503 the volume of water that overflows the riverbanks into the floodplains as the flood wave propagates
504 along the river network. The main river channel and the floodplains can have significantly different
505 roughness characteristics, due to the different landuse and land cover in the watershed.

506 UWR has a higher roughness in the floodplains because its floodplains are dominated by
507 forests, shrubs and agricultural lands which have Manning's n in the range of 0.18 – 0.24.
508 Therefore, the water inundating into the floodplains experiences higher frictional forces thereby
509 reducing the flow velocity in the floodplain when compared to the water in the main channel
510 (Manning's n: 0.035). The difference in channel conveyance capacities of M1, M2 and M3 lead to
511 differences in the partitioning of flood wave between the main channel and the floodplains, which
512 in turn leads to differences in the flow hydrographs at the outlet. For example, the 2016 simulation
513 in UWR is a relatively small event where most of the water stays within the banks for Control, M1

514 and M2. However, M3's inadequate conveyance capacity leads to a higher volume of water
515 flowing through the floodplains. Figure 10(a) shows that the peaks for M1 and M2 are similar to
516 those of Control, whereas M3's peak is delayed by 24 hours as compared to Control (for the peak
517 observed on 15th March 2016 (day 22)) due to slow propagation of the excess water flowing
518 through the floodplains. In the case of WHR, 89% of the floodplains (Table 1) are developed and
519 have a smaller roughness (Manning's *n*: 0.011 – 0.015). A higher percentage of developed
520 (impervious) region causes the rainfall-induced surface runoff to travel through the floodplain
521 faster before reaching the river channels, thereby, resulting in increased flow at the outlet as shown
522 in Figure 10(c).

523 It is expected that the configuration with higher bathymetric detail should perform better
524 and that the performance should reduce with decreasing levels of bathymetric detail. However, for
525 small within-channel events (< 2-year return periods) such as those in the 2016 simulation at UWR
526 and the 2015 simulation at WHR, the decrease in model performance from M1 to M2 is negligible
527 as compared to the decrease in model performance from M2 to M3. The additional channel
528 conveyance in M2 as compared to M1 (and Control) does not adversely affect model performance
529 since most of the flow is confined to the channel and the volume of water flowing through the
530 floodplains is minimal. For medium-sized events (> 2-year events but < 25-year event) such as the
531 2018 event in UWR, the partitioning of water becomes more important and both overestimated
532 (M2) and underestimated (M3) channel conveyance leads to poorer model performance. For
533 example, the RSR (Table 6) is 0.24 and 0.27 for M2 and M3, respectively while M1 has a better
534 RSR of 0.16. In the case of events with much higher magnitude of streamflow (>50-year return
535 period), the impact of additional channel conveyance and increased slope is less significant as the
536 proportion of water in the main channel is relatively small when compared to the floodplains.

Therefore, for high magnitude flow, it can be argued that the difference in the volume of water routed through the floodplains for different configurations becomes insignificant resulting in similar model performance.

In terms of maximum inundation extent, estimates of M1 are close to those of Control. M2 has a higher channel conveyance capacity than Control which leads to a smaller inundation area whereas M3 has a smaller channel conveyance capacity than Control leading to an overestimation in the maximum inundation area. This behavior is consistent with previous findings on the effect of bathymetry on inundation extent (Dey et al., 2019; Grimaldi et al., 2018). One notable exception is M3 for 2018 simulation in UWR, where the overestimation in inundation area due to low channel conveyance capacity is countered by the lower peak in outlet hydrograph leading to similar inundation area estimates for M3 and Control.

Overall, the results indicate that depth (slope) and channel conveyance (cross-sectional area), irrespective of the shape, act as important controls for overland flow especially for medium-sized events and that the error due to overestimating channel conveyance reduces for small within bank events. Typically, hydrologic and hydrodynamic model parameters are calibrated against observed hydrographs at gauged locations. In the absence of bathymetry and adequate model physicality, such calibration would have resulted in the lack of channel storage in the river network being compensated by parameter values that characterize other physical processes. For example, in the absence of river bathymetry, an alternate approach is to assume simplified cross-sectional shapes to develop a hydrodynamic model and calibrate the depth of these cross-sections and the roughness characterization in the hydrodynamic model using observed hydrographs, stage or rating curves (Gichamo et al., 2012; Grimaldi et al., 2018; Neal et al., 2015; Price, 2009). Such an approach will not account for the effect of river bathymetry (depth) on streamflow generation

560 processes such as infiltration and lateral seepage. Instead, the calibrated values of depth and
561 roughness try to compensate for the inaccurate representation of fluvial processes which may lead
562 to additional error in the model when simulating different events. To further investigate these
563 issues, the subsequent sections compare the estimates of infiltration, lateral seepage, backwater
564 flow and inundation area between different bathymetric configurations. This will determine if the
565 difference in watershed response to bathymetric representations is limited to surface routing only
566 or if its effect extends to other fluvial processes such as SW-GW interactions.

567 *6.4 Effect on Infiltration*

568 Results, presented in Figure 11 and Table 7, show that difference in infiltration rates
569 estimated by M3 with respect to Control is the highest, followed by M2 and M1 which indicate
570 that increasing bathymetric detail also improves the estimation of daily infiltration rates. M3's
571 performance is particularly poor which is reflected in the negative and near-zero NSE values. The
572 estimates of daily infiltration rate improve drastically from M3 to M2, with a relatively smaller
573 improvement from M2 to M1 as indicated by the increasing values of NSE and decreasing values
574 of RSR (Table 7), which is similar to the behavior of SW fluxes during a flood event (Section 6.3).

575 **Table 7**. Performance metrics comparing the daily infiltration rates in the floodplain estimated
576 by M1, M2 and M3 with respect to Control

Simulation	Configuration	NSE	Pbias (%)	RSR	Error in Peak (%) *
UWR (2016)	M1	0.98	-2.2	0.14	-5.24
	M2	0.86	-8.9	0.38	5.94
	M3	-3.19	59.3	2.03	74.14
UWR (2018)	M1	0.86	-14.8	0.37	-11.95
	M2	0.71	-22.0	0.54	-14.51
	M3	0.02	37.3	0.98	14.26
WHR (2015)	M1	0.84	1.6	0.39	21.96
	M2	0.47	-7.3	0.71	20.75
	M3	-0.40	23.5	1.16	35.70

577 *Error in peak corresponds to the highest peak in the simulation period

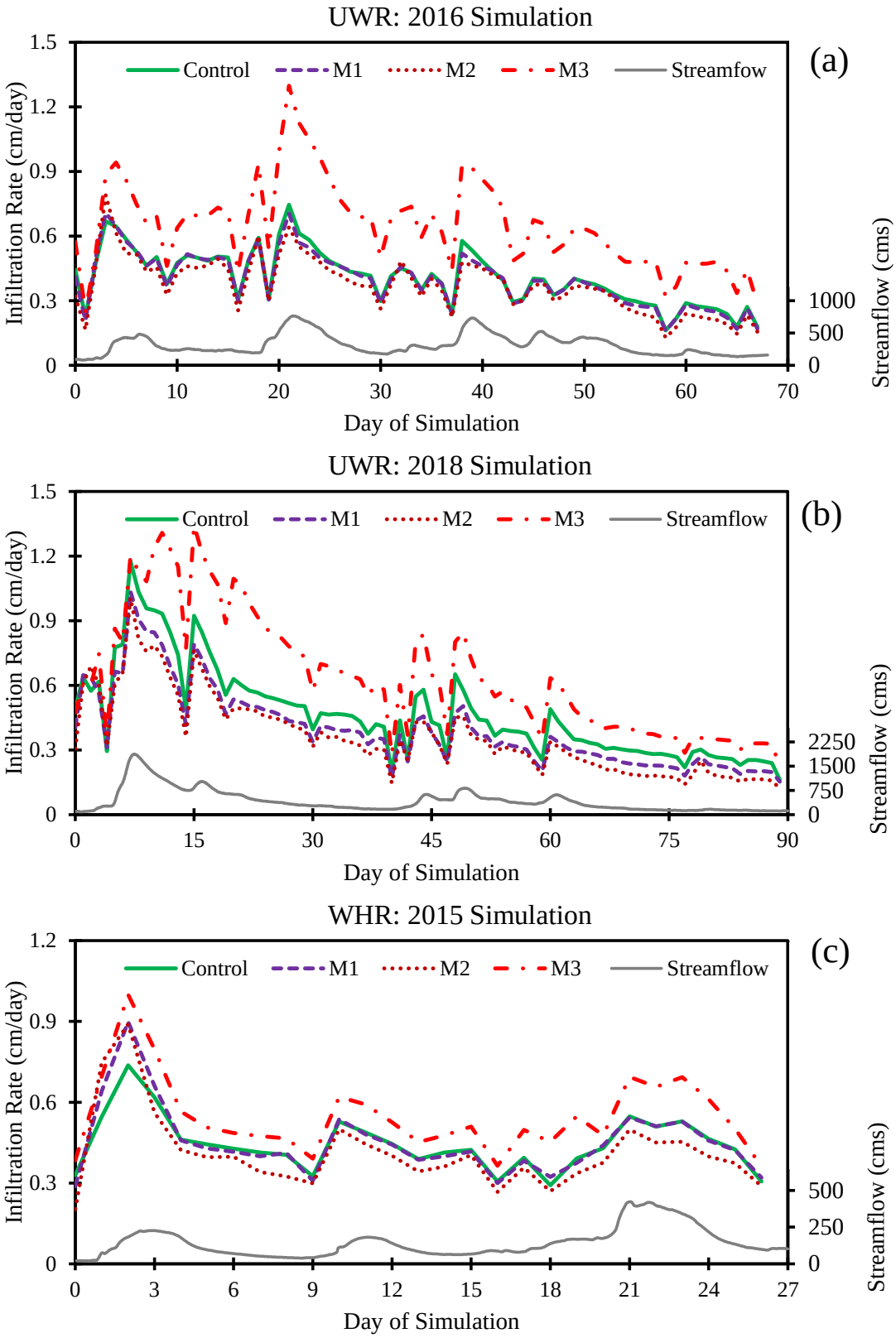

Figure 11: Daily infiltration rate in the floodplains of UWR for (a) 2016 simulation, (b) 2018 simulation and (c) WHR for 2015 simulation. The observed outlet hydrograph is shown in grey line on secondary axis.

582

583 Initially, as seen in Figure 11, the infiltration rates are similar for all configurations because
584 the flow is confined to the saturated river channels. As the flood waves travel through the stream
585 network, the lateral SW flux from the river channels to the floodplains increases. As demonstrated
586 using a conceptual diagram in Figure 12, the SW flux into the floodplains is controlled by the
587 channel conveyance capacity of the river network. High conveyance capacity not only leads to
588 lower floodplain storage but also reduces the total volume of water available for infiltration into
589 the subsurface leading to lower rates of infiltration and vice-versa. This effect can be seen in all
590 three events, where M3 (lower channel conveyance capacity) is consistently overestimating the
591 infiltration rate whereas M2 (higher channel conveyance capacity) is consistently underestimating
592 the infiltration rates with respect to Control. M1 has a similar channel conveyance capacity to
593 Control and is performing the best as evident from its high NSE.

594 Further, once the flood wave starts receding, the SW fluxes recede from the floodplain
595 back into the river channels. In this case, higher channel conveyance allows the water to recede
596 faster from the floodplains leading to smaller residence times for surface water in the floodplains
597 which further maintains the difference in the total infiltration volume even in the receding part of
598 the flood event. This effect can be seen in Figure 11(b) where there are differences between the
599 infiltration rates of the three configurations from Control even after the flood wave recedes, for
600 example, between Day 30 (24th March 2016) and Day 36 (30th March 2016) for the 2016 event and
601 between Day 25 (12th March 2018) and Day 35 (22nd March 2018) for the 2018 event in UWR.

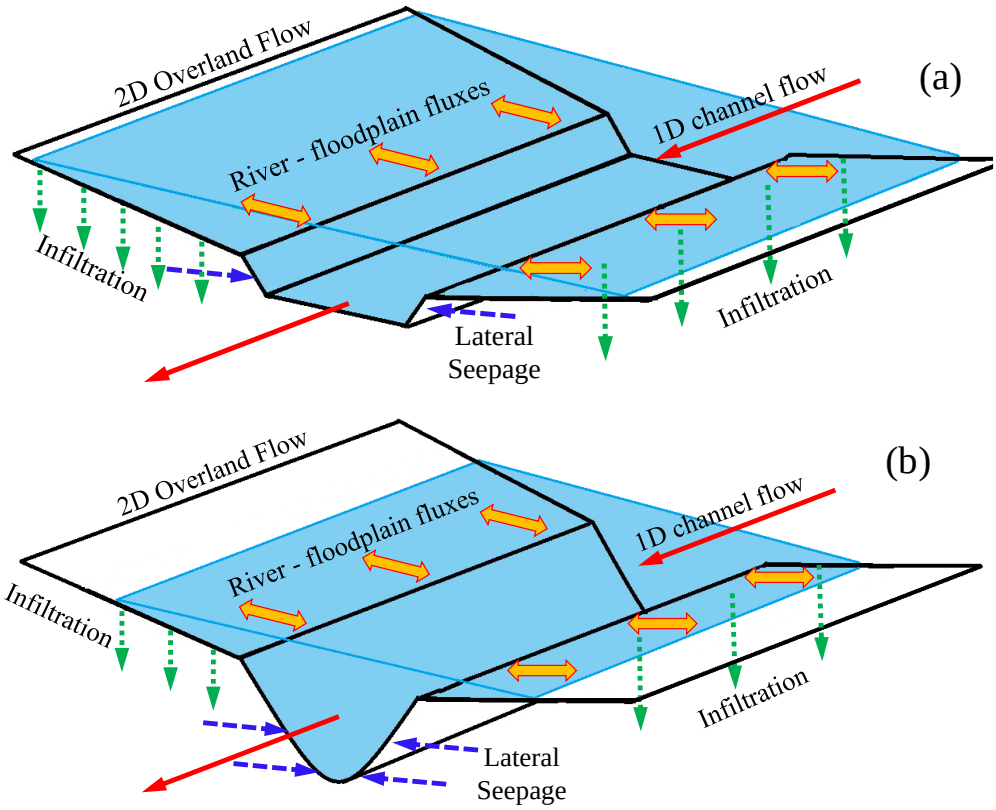

Figure 12. Conceptual figure illustrating the difference in physical processes between two bathymetric configurations with (a) low and (b) high channel conveyance capacities. Low channel conveyance capacity leads to a higher inundation area, WSE and infiltration and lower lateral seepage as compared to a bathymetric configuration with higher channel conveyance capacity.

In case of WHR (Figure 11(c)), the infiltration rates estimated by M1, M2 and M3 exhibit a similar trend to that of UWR – M1 is closest to Control with M2 underestimating the infiltration rate and M3 overestimating the infiltration rate. However, the difference between the estimates produced by the different bathymetric configurations is smaller for WHR when compared to UWR. This variation in WHR can be attributed to the different landuse patterns in the floodplains of WHR. There is a higher percentage of developed area in the floodplains (Table 1) of WHR leading to a lower available subsurface storage and lower infiltration capacity in the floodplains. Additionally, the water flows faster through the floodplains because of the lower roughness in developed regions allowing the water in the floodplains to recede faster into the main channel after

the flood peak passes through the river network. These two factors together lead to a smaller difference between the estimates of the different bathymetric configurations in case of WHR than in UWR.

It is evident that the effect of improper bathymetric representation is not limited to SW processes but also affects SW-GW interactions such as infiltration which can, in turn, affect the rainfall-runoff in a watershed since there is bi-directional feedback between these two processes. However, loosely coupled hydrologic and hydrodynamic models (Afshari et al., 2018; Follum et al., 2020; Rajib et al., 2020; Wing et al., 2017) neglect such feedbacks which may get compounded by improper bathymetric representation. Errors in bathymetric representation combined with simplistic routing procedure in the hydrologic model may lead to erroneous estimates of infiltration and streamflow which can propagate through the hydrodynamic model.

6.5 Effect on Lateral Seepage

The net lateral seepage is calculated as the difference in cumulative lateral seepage inflow and outflow for each day of the simulation. As such, a negative lateral seepage indicates that the river network is losing water into the subsurface, whereas a positive lateral seepage indicates that the river network is gaining water from the subsurface.

As shown in Figure 13, the net lateral seepage is negative during the flood event as a large volume of water seeps into the subsurface due to higher heads in the river channels. However, after the flood wave recedes, the net lateral seepage becomes positive as the water that has seeped into the subsurface during the event starts recharging into the river channels. M1 provides decent estimates of lateral seepage rate when compared to Control, as is evident from high NSE, low RSR and low error in peak lateral seepage rate. M2’s performance is even worse than M3's. It has a

640 negative NSE for the 2018 event in UWR and exhibits large biases in the positive direction for all
641 three events.

642 **Table 8**. Performance metrics comparing the daily net lateral seepage rate in the floodplain
643 estimated by M1, M2 and M3 with respect to Control

Simulation	Configuration	NSE	Pbias (%)	RSR	Error in Peak (%) *
UWR (2016)	M1	0.97	20.8	0.16	17.44
	M2	0.32	183.0	0.82	57.83
	M3	0.61	-69.8	0.62	26.71
UWR (2018)	M1	0.99	-7.2	0.10	-3.13
	M2	-1.01	258.6	1.41	53.39
	M3	0.90	-6.1	0.32	5.70
WHR (2015)	M1	0.87	-24.3	0.35	-3.91
	M2	0.30	-65.0	0.82	-23.10
	M3	0.40	-50.0	0.76	-50.00

644 *Error in peak corresponds to the highest peak in the simulation period

645

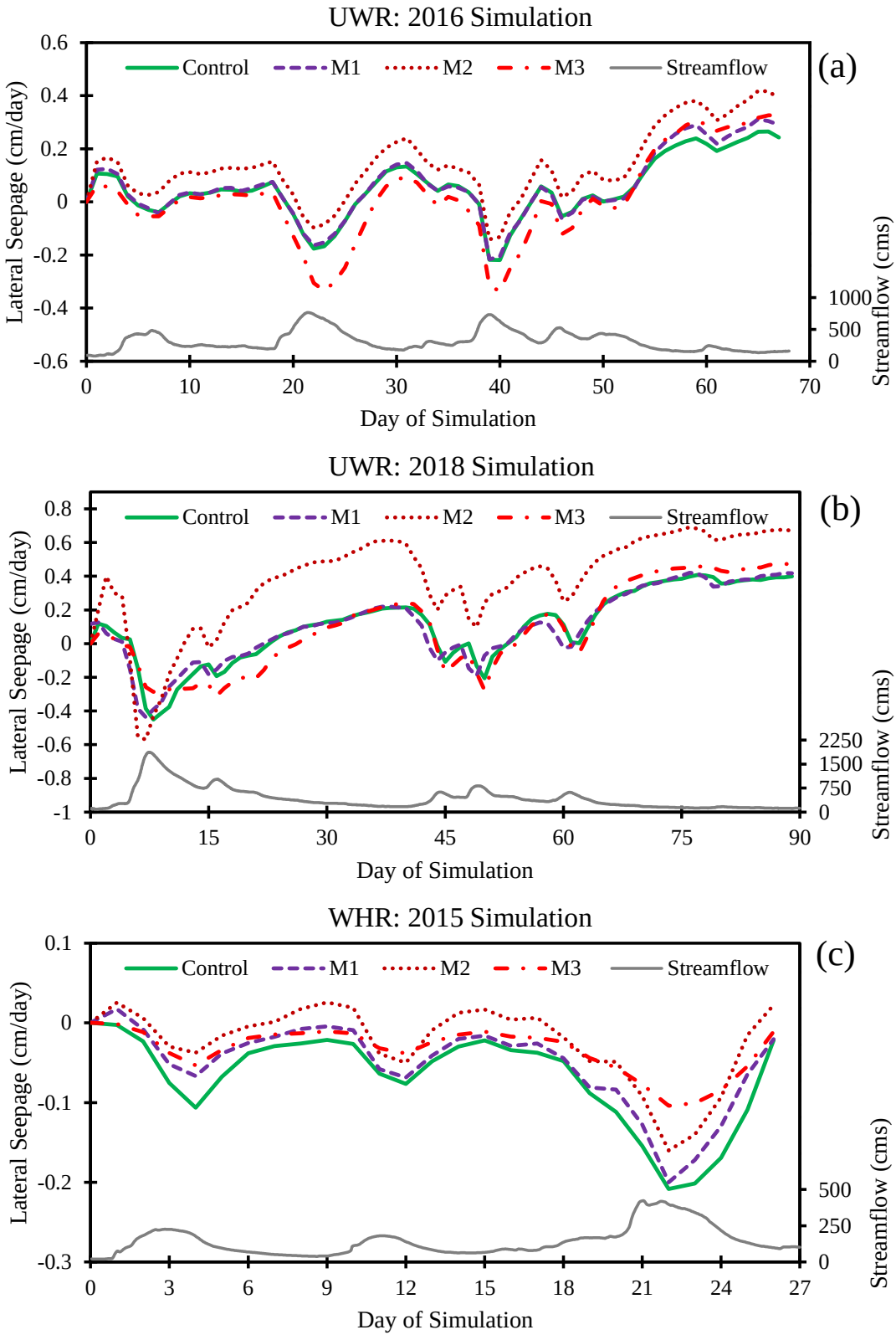

Figure 13: Daily lateral seepage rate in the floodplains of UWR for (a) 2016 simulation, (b) 2018 simulation and (c) WHR for 2015 simulation. The observed outlet hydrograph is shown in grey line on secondary axis.

650 The lateral seepage is controlled by the saturated area available for the exchange of fluxes
651 between the river channel and GW and the head distribution in the channel and floodplains. As the
652 flood wave propagates along the channel network, it pushes the old water in the channel as well
653 as the GW in the floodplains away from the river channel. Similarly, as the water in the channel
654 recedes, it creates a pulling effect that forces water from the surrounding GW in the floodplains to
655 rush to the river channel. This leads to a high correlation between GWT elevation in the river
656 channel and river channel heads (Jung et al., 2004). The WSE in the river channel is governed by
657 both the volume of water flowing through the channel and the channel geometry (bathymetry).
658 The overall channel bed elevations for M2 are lower than that of Control. It also has the highest
659 channel conveyance capacity. WSE in the channel is lowest for M2, followed by those of Control
660 and M1 and finally, M3 has the highest WSE. Lower the WSE in the channel, lower the SW head
661 in the channel driving the lateral seepage. This leads to a less negative (more positive) lateral
662 seepage rate for M2. This also explains the more negative estimates of M3 which has the lowest
663 channel conveyance capacity and highest WSE of the three configurations. A similar scenario is
664 observed for WHR, but a smaller difference in net lateral seepage is observed between the different
665 bathymetric configurations due to WHR having a primarily developed landuse leading to limited
666 SW-GW interactions.

667 The saturated surface area in the river network (wetted perimeter in a cross-section)
668 available for SW-GW exchange also plays a role in controlling the lateral seepage. M1 and M2
669 have the same surface area but different channel conveyance capacity leading to significantly
670 different performance in terms of lateral seepage rates. Also, as shown in Table 3, the difference
671 in surface areas between the configurations is not as high as the difference between channel
672 conveyance capacity. This indicates that incorporating channel geometry with accurate channel

673 conveyance capacity may suffice in accurately capturing the SW-GW processes for medium to
674 large watersheds.

675 In this study, Control incorporates the thalweg variability along a river network leading to
676 better representation of thalweg-gegenweg and side slopes as recommended by Chow et al., (2018)
677 and Doble et al., (2012), respectively to model the lateral seepage. The differences between
678 estimates of Control and M1 (vertical side slopes and symmetric river channel geometry) are
679 relatively small which indicates that these two bathymetric characteristics play a minor role in
680 lateral seepage across large river networks. More importantly, the stark difference in the
681 performance of M1 and M2 relative to Control indicates that channel conveyance capacity has a
682 greater effect on the SW-GW fluxes at larger spatial domains incorporating river corridor or river
683 networks (and beyond).

684 *6.6 Effect on Groundwater Table*

685 As shown in the previous sections, the incorporation of river bathymetry, specifically the
686 channel conveyance, has a significant impact on subsurface processes such as infiltration and
687 lateral seepage. Since both these processes are related to available subsurface storage, which is
688 subsequently dependent on the water table depth, the effect of incorporating bathymetry on GWT
689 elevation is analyzed in this section by comparing the maximum GWT elevation estimated by the
690 three configurations with Control as shown in 13. The differences in maximum GWT elevations
691 (ΔGWT_{max}) has been corrected for biases due to initial conditions as per the following equation
692 (Equation 5).

693 $$\Delta GWT_{max,Mi} = GWT_{Control,max} - GWT_{Mi,max} - (GWT_{Control,initial} - GWT_{Mi,initial})$$

694 (Equation 5)

where $\Delta GWT_{\mathrm{max,Mi}}$ is the bias-corrected difference in maximum water table elevations estimated by the bathymetric configuration Mi (M1, M2 or M3) and Control, and $GWT_{Control,initial}$ and $GWT_{Mi,initial}$ are the initial water table elevations for Control and M*i* (M1, M2 or M3) respectively. Areas with a positive value of $\Delta GWT_{max,Mi}$ for a given configuration have a higher change in water table elevation for Control as compared to that configuration while negative values of $\Delta GWT_{max,Mi}$ indicate that the region has a higher change in water table elevation for that configuration compared to Control. If $|\Delta GWT_{max,Mi}| < threshold$, then that region is said to have no meaningful difference in the maximum water table elevations estimated by M1 and M2. The *threshold* is implemented for filtering out small differences caused due to model discretization and conversion between unstructured mesh and gridded data. In this study, the *threshold* is set to 0.15m (6 inches) – an arbitrarily chosen value based on prior modeling experience. Since the only difference in the different configurations is the bathymetric representation, analyzing ΔGWT_{max} across the study area demonstrates the spatial distribution of the effect of river bathymetry on GW processes.

Figure 14 shows the areas in UWR where the maximum water table elevations are significantly different for the three configurations compared to Control for the 2018 simulation. M1 has the least differences in ΔGWT_{max} compared to M2 and M3 as evident with a lesser percentage of green and red zones in Figure 14. M2 and M3 have contrasting distributions of ΔGWT_{max} in the floodplains. M2 has a higher percentage of areas with positive ΔGWT_{max} whereas M3 has a higher percentage of negative ΔGWT_{max} in the floodplains with the positive ΔGWT_{max} mostly confined to the main river channel. This difference in the distribution of ΔGWT_{max} for M2 and M3 can be attributed to differences in infiltration and lateral seepage rates of M2 and M3 (Section 6.4 and 6.5). The infiltration rate of M2 is lower than Control which means

M2 has a lower volume of water infiltrating into the GW leading to lower changes in GWT elevation as compared to Control leading to positive ΔGWT_{max}. On the other hand, M3 has a higher infiltration rate than Control leading to higher changes in GWT with respect to Control leading to negative ΔGWT_{max}. The difference in lateral seepage also further enhances the difference between Control and M2 or M3. M2 has a more positive lateral seepage which indicates that the river channel is gaining more (losing less) water from the GW, leading to smaller changes in GWT whereas M3 has a more negative lateral seepage indicating the stream losing more water, which causes higher changes in GWT in the floodplains. However, the volume of water being lost/gained due to lateral seepage is small as compared to the volume of water being gained through infiltration.

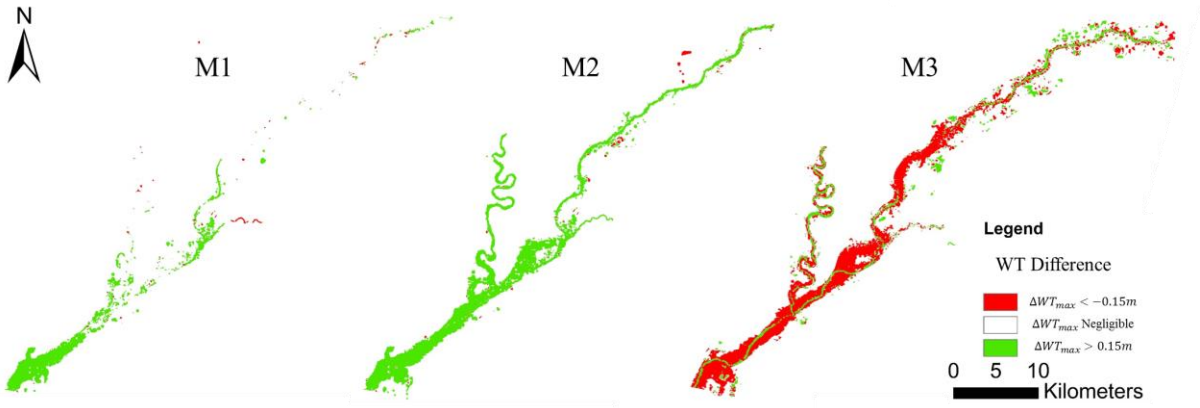

Figure 14. Figure showing the spatial distribution of differences between change in water table elevations estimated by the different bathymetric configurations and Control at Wabash River Basin (UWR). Green regions have a positive ΔWT_{max} which indicates that those regions have lower changes in water table elevation from initial water table elevations for a given bathymetric configuration as compared to Control, and vice-versa for the red regions.

The spatial distribution of ΔGWT_{max} also highlight the fact that the effect of bathymetric configuration on GWT is spread throughout the network and is not limited to the main stem of the river. Additionally, it highlights the fact that there is a need for incorporating the channel

conveyance capacity accurately since both underestimation (M3) and overestimation (M2) of channel conveyance capacity leads to significant differences in estimates of GWT elevation. This may be particularly relevant in the field of contaminant transport, wetland modeling and stream restoration (Banks et al., 2011; Cienciala and Pasternack, 2017; Czuba et al., 2019; Osman and Bruen, 2002).

Traditional hydrodynamic modeling cannot reflect the change in flow volume due to within-reach hydrologic processes. Therefore, hydrodynamic models have only been able to highlight the effect of poor bathymetric representation on SW fluxes. However, flooding-related physical processes are codependent on each other; they continuously influence each other directly or indirectly through feedback loops. The results presented in this study show that the impact of bathymetry is not limited to surface fluxes but also extends to subsurface processes and SW-GW interactions. Effective incorporation of bathymetric representation in data-sparse regions should focus on accurately estimating bathymetric characteristics rather than on the overall shape of the channel geometry. Specifically, the focus should first be on incorporating accurate estimates of channel conveyance capacity and thalweg elevation, followed by side slopes and channel asymmetry for accurately simulating the SW-GW processes in floodplains for river networks at large spatial domains.

6.7 Effect on Backwater Flow at Confluence

At a river confluence, the two streams draining to the confluence may not have similar thalweg elevation, especially when lower order streams meet a higher order stream. Usually, the main river is deeper than the tributary, and the difference in thalweg elevation increases as the difference in the stream orders of the main river and its tributaries increases. This difference in thalweg elevation can affect the flow patterns near a confluence but this effect is usually ignored

762 in traditional hydraulic models. To investigate this effect, the streamflow hydrograph just upstream
763 of the confluence is compared for M1, M2 and M3 against Control. Figure 15(a) shows the
764 hydrograph at the downstream end of Wildcat Creek as it drains into the Wabash River. The figure
765 shows that Wildcat Creek experiences backwater flow (negative flow) from the Wabash River on
766 days 22 to 24 of the simulation (16th March 2015 to 18th March 2015) in case of M3, whereas M1
767 and M2 do not exhibit this backflow – same as Control. This indicates that the backwater is
768 spuriously induced by the incomplete representation of bathymetry in M3.
769

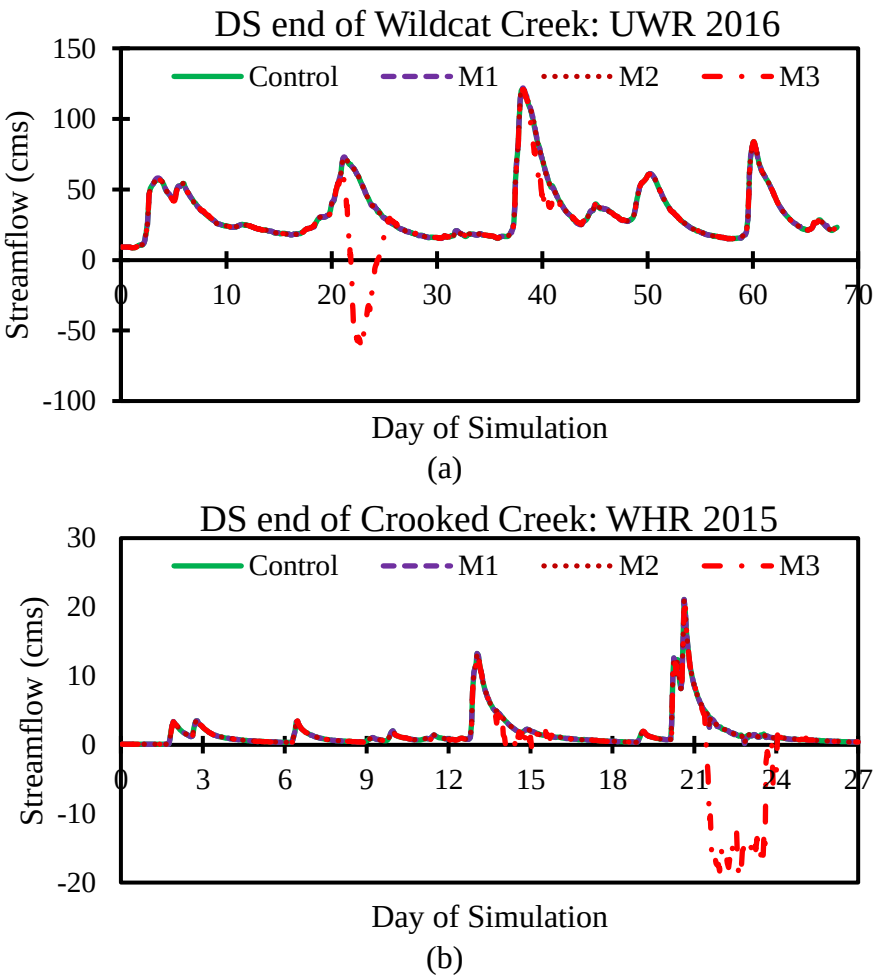

770

771 **Figure 15.** Figure showing hydrographs at the downstream (DS) end of tributary at (a) the
772 Wildcat Creek – Wabash River confluence (UWR) and (b) the Crooked Creek – White River
773 confluence (WHR) for all three configurations.

774

775 All three configurations (M1, M2 and M3) have differences in bathymetric characteristics.
776 M3 is based on the original Lidar where the entire river network is characterized by a flat surface
777 with a very mild longitudinal slope. The thalweg elevations are the same for Control, M1 and M2
778 but are different from those of M3. The fact that only M3 is exhibiting such a behavior can be
779 attributed to the difference (or lack thereof) in thalweg elevation of the main stem and the tributary.
780 In case of Control, M1 and M2, the thalweg is higher for Wildcat Creek (155.7 m) as compared to
781 Wabash River (154.8 m) at the confluence, which acts as a barrier to the flow of water from
782 Wabash River to Wildcat Creek, thereby reducing the backwater flow in the channel. This
783 elevation difference between Wabash River and Wildcat Creek is not present in M3 where the
784 thalweg elevation for both the channels is 156.2 m. This allows the water from the Wabash River
785 to travel upstream along Wildcat Creek, thereby leading to backwater flow. A similar effect can
786 also be observed in WHR at the confluence of Crooked Creek and White River, as demonstrated
787 by Figure 15(b) where Control, M1 and M2 have a difference of 0.7 m in the thalweg of Crooked
788 Creek and White River at the confluence but M3 has no difference in thalweg elevation at the
789 confluence.

790 This difference in flow patterns is not observed at every confluence. For example, the
791 difference in flow at the downstream end of the Tippecanoe River (just upstream of the Wabash-
792 Tippecanoe confluence) is negligible. The Wabash River – Tippecanoe River confluence has a
793 smaller difference in thalweg elevation at the confluence (0.5m) than the Wabash River – Wildcat
794 Creek confluence (0.9 m). Figure 15 also shows that the backwater flow exists for only one of the
795 peaks at the Wabash River – Wildcat Creek confluence. This difference in behavior can be
796 explained by the relative difference in magnitude of flow along the tributary and the main channel.

797 Surface routing of water is governed by the total head of water, which in turn, depends on the
798 thalweg elevation and water depth. The water depth depends on the volume of water flowing
799 through the channel. If the flood wave traveling along a tributary is comparable to the flood wave
800 of the main river at the confluence, the flood wave in the tributary may act as a further barrier to
801 backwater flow. This may compensate for the lack of difference in thalweg elevation in M3 and
802 impede backwater flow. Therefore, the relative size of the channels meeting at a confluence and
803 the difference in flow through them may be responsible for the backwater effect to be important at
804 confluences.

805 If two streams at a confluence have a large difference in thalweg elevations of main channel
806 and tributary or the events are of different magnitudes, the absence of bathymetry at confluences
807 can result in highly erroneous streamflow at the watershed outlet due to backwater flow. The
808 spurious backwater flow in the absence of bathymetry can lead to erroneous localized flooding
809 around the confluence. Therefore, confluence geometry with appropriate representation of
810 differences in thalweg elevations between the tributary and main river at the confluence must be
811 incorporated to ensure accurate hydrodynamic connectivity along the river network, particularly
812 for large-scale applications spanning large networks which have confluence between rivers with
813 markedly different bed elevations (Mejia and Reed, 2011; Tran et al., 2020; Trigg et al., 2009).

814 **7. Summary and Conclusion**

815 Bathymetry is critical for accurate modeling of fluvial systems. However, traditional river
816 modeling has focused on evaluating the effect of bathymetry on surface routing processes along
817 single reaches, usually the main stem of the river network. Fluvial systems comprise of co-
818 dependent surface and subsurface physical processes which affect hydrodynamic variables
819 significantly, especially at large watershed scales. This study evaluates if the effect of river

bathymetry extends beyond surface processes to subsurface processes such as seepage and infiltration. Additionally, the study analyzes the bathymetric characteristics that control these processes to provide insights into effective ways to incorporate bathymetry across large river networks in data-sparse regions. To answer these research questions, a conceptual bathymetric model, SPRING, which can generate bathymetry for entire river networks, is implemented on two watersheds with distinct physical characteristics (agricultural and urban). Physically-based distributed models are created for four different bathymetric configurations with successively reduced bathymetric detail: Control (highest level of detail – calibrated asymmetric cross-sections with realistic side slope), M1 (depth, channel conveyance capacity and vertical side slope), M2 (depth and vertical side slope) and M3 (original Lidar with no additional bathymetric detail). Analysis of hydrologic and hydrodynamic outputs from the four configurations leads to the following conclusions:

1) The application of SPRING in the Wabash (UWR) and White River (WHR) basins demonstrate its ability to estimate bathymetry for tributaries as well as the main river stem in a river network. Additionally, it can maintain hydraulic connectivity among channels with proper representation of bathymetry at confluences. Bathymetry incorporation can lead to a significant increase in channel conveyance capacity across the river network and overall longitudinal slope of the channel but the change in the surface area remain relatively small.

2) A comparison of the streamflow prediction at the outlet using the four configurations indicates that depth (slope) and channel conveyance (cross-sectional area), irrespective of the shape, play an important role in accurately simulating flood events across river networks. Channel conveyance capacity controls the partitioning of the flood wave between the main channel and the floodplains. Because of a significantly different roughness distribution in the floodplain compared

to the main river channel, the water routed through the floodplains can either slow down or speed up (depending on the land use in the floodplain). While the absence of bathymetry leads to poor performance for all events, small events may be captured accurately by incorporating accurate channel depth (thalweg elevation) only. However, for medium-sized events, both channel conveyance and depth need to be incorporated for adequately capturing the watershed response.

3) The impact of bathymetry on subsurface processes is demonstrated by the difference in infiltration rates across the four configurations. The infiltration rates remain similar when the channel conveyance capacity and depth are adequately incorporated. In the absence of adequate bathymetric detail, lower (higher) channel conveyance capacity causes higher (lower) influx of water into the floodplain during flood events, which increases (decreases) the floodplain residence time, thereby increasing (decreasing) the infiltration. The influence of bathymetry in infiltration is also affected by the landuse of floodplains, with developed regions showing lesser but still significant differences in infiltration.

4) Lateral seepage depends on the head distribution in the river network and the saturated area available for SW – GW interaction. A higher channel conveyance capacity lowers the water surface elevation and may increase the wetted area in the river network. Therefore, it leads to increased seepage from the GW into the channel, and its underestimation leads to overestimation in seepage from the channel into the GW. Lateral seepage is particularly sensitive to bathymetric detail as the result demonstrated that incorporating inaccurate channel conveyance can lead to even poorer estimates of lateral seepage as compared to not incorporating any bathymetric information.

5) The differences in infiltration and lateral seepage rates due to bathymetric configurations contribute to significant differences in water table elevations throughout the river network. Lack of bathymetry, especially underrepresenting the channel conveyance capacity can lead to

866 overestimation in water table elevations and vice-versa. This indicates that errors in bathymetry
867 can propagate to surface and subsurface processes as well as the interaction between these
868 processes.

869 6) The overall performance of the bathymetric configurations across both watersheds
870 indicate that channel conveyance capacity and thalweg elevation (longitudinal slope) play a critical
871 role in accurately capturing both surface and subsurface processes in H&H models. Therefore, in
872 estimating conceptual bathymetry for data sparse regions, the focus should be on incorporating
873 accurate channel conveyance and thalweg elevation. Additional information regarding channel
874 side slope and channel asymmetry may further improve the accuracy of H&H model.

875 7) The bathymetry at river confluences plays a critical role in determining the flow patterns
876 in the region. In the absence of bathymetry, the tributary may experience significant backwater
877 flow. After bathymetry incorporation, the thalweg elevations of the main channel and tributary just
878 upstream of the confluence may be significantly different. This acts as a barrier to backwater flow
879 from the main channel moving upstream of the tributary. This effect seems to be localized to the
880 vicinity of the confluences and the extent of backwater flow also depends on the relative size and
881 timing of the flood wave arriving at the confluence from the tributary and main river.

882 **8. Limitation and Future Work**

883 This study demonstrates the effect of incorporating bathymetry across large river networks
884 on watershed processes using physically-based distributed modeling. There are certain limitations
885 to the results presented here. While the proposed framework for generating bathymetry (SPRING)
886 can be applied to every reach including lower-order streams, this study only analyzes the effect on
887 the main stem and three of its major tributaries at both sites. This is primarily due to the lack of
888 accurate thalweg elevations and channel volumes across the river network. Since accurate depth

and channel volume are critical to generating accurate bathymetry, future studies should focus on estimating these bathymetric characteristics for all channels in a network. In this regard, remote sensing-based methods such as the FREEBIRD algorithm, hydraulic modeling based depth/volume calibration, or remote sensing-based at-a-station equations may be particularly useful (Grimaldi et al., 2018; Legleiter et al., 2011; Price, 2009). Additionally, implementing SPRING for large-scale application across river networks spanning hundreds or even thousands of kilometers requires the automated generation of input datasets such as river centerline and banks. While public datasets such as the National Hydrography Database (NHD) do exist, they suffer from inaccurate spatial correspondence with the DEM. Such large-scale implementation necessitates the use of high-performance computing and parallelization. Therefore, future work also includes developing an automated and efficient algorithm that can create these input datasets for SPRING and use parallelization methods for computational efficiency at large scales. Additionally, large-scale application of SPRING also requires evaluation of the data requirements of calibrating the parameters of SPRING as well as spatial transferability of the parameter set across different river networks.

The results presented here indicate that the difference due to bathymetry incorporation may be dependent on the scale of the main river, its tributaries, the magnitude and intensity of the event, and overall spatial extent and landuse distribution of the watershed. Future forays in this direction should consider researching the appropriate spatial scales at which the impact of bathymetry becomes more or less significant in the context of hydrologic and hydraulic processes. This may provide insights into when and where bathymetry incorporation is necessary and if there exist circumstances where bathymetry incorporation may be neglected for certain streams. This is particularly important in the context of developing large-scale accurate flood models.

Acknowledgments and Data

This work was performed with funding from the U.S. National Science Foundation (Grants 1706612, 1737633, 1835822). Any opinions, findings, and conclusions or recommendations expressed in this material are those of the authors and do not necessarily reflect the views of the National Science Foundation.

SPRING is available for implementation as an ArcGIS toolbar. The installer and instruction manual are shared in HydroShare at: https://www.hydroshare.org/resource/5f997ec440ea41859bc329ea4a5d7289/. All data used in this study will be made available in HydroShare upon acceptance of the manuscript for publication.

Appendix A1: Estimating river bathymetry at individual reaches

This section gives a brief explanation of the procedure followed by SPRING to estimate river geometry for individual reaches. For more details, please refer to Dey, (2016) or Merwade, (2004).

For each river reach in the network, the channel centerline is divided into small segments, which are 10-14 times the width of the channel. The depth at each of these segments is estimated by linearly interpolating between the known depth at the USGS gage locations within the river network. For each segment, a normalized cross-section is created which has unit width and unit depth. First, the radius of curvature (r) of the centerline segment is estimated using the three-point arc method. Then the width of the channel (w) is calculated by measuring the average distance between the banks for that centerline segment. The thalweg position (t), which is the distance of the thalweg from the channel centerline along a river cross-section, is determined using an exponential function relating the normalized radius of curvature ($r^* = r/w$) to normalized thalweg position ($t^* = t/w$) as shown in Equation 1. The sign of the thalweg position (left of centerline: negative, right of centerline: positive) is determined by the direction in which the river meanders. If the river meanders (turns) to the left, there is more erosion on the right bank (outer bank) and more deposition on the left bank (inner bank). Consequently, the thalweg is positioned on the right side of the centerline (positive thalweg location). SPRING determines the position of the thalweg by locating the center and radius of curvature of the meander using the three-point rule. If the center of curvature of the meander is to the left of the centerline, the thalweg is located on the right side of the centerline, that is, the thalweg position is positive and vice-versa. In summary, the position of the center of curvature of the meander relative to the centerline

945 determines the sign (direction) of the thalweg position and the radius of curvature determines the
946 distance between the centerline and the thalweg position.

947 Finally, asymmetric cross-sections having unit depth and unit width are estimated based
948 on the thalweg position, using a linear combination of beta-functions as shown in Equation 2. The
949 scaling parameter, k, in Equation 2 is introduced in the equation to remove the constraint of total
950 area in a cross-section. The area under a pdf is always equal to 1, so the area under the sum of two
951 pdfs cannot be greater than 2. However, this constraint is not applicable to a normalized river
952 cross-section of unit width and unit depth. The introduction of scaling parameter in the equation
953 removes the area constraint and increases the flexibility of SPRING to create cross-sections of
954 different shapes. The parameters of SPRING can be estimated from surveyed cross-sections
955 available for a different section of the same river or from a different river with similar
956 characteristics as the river in question. Finally, the width and bank elevation of the river channel
957 for that segment is estimated using the bank lines and DEM. These are used to rescale the
958 normalized cross-section shape to actual cross-section using Equation 3. After creating cross-
959 sections for each centerline segment using SPRING, longitudinal 3D lines (called profile lines) are
960 drawn along the channel intersecting the cross-sections. Channel bed elevations are interpolated
961 between the estimated cross-sections along these profile lines in a channel centered curvilinear
962 coordinate system (Glenn et al., 2016; Merwade et al., 2006) to create a 3D mesh depicting the
963 channel bathymetry.

964

Appendix A2: Integrated Channel and Pond Routing

This section provides supplementary information on the computational framework used in Integrated Channel and Pond Routing (ICPR), a physically based tightly coupled distributed model capable of simultaneously estimating flooding related surface and subsurface processes in a watershed. Information provided in this section has been adapted from Saksena et al., (2021, 2020, 2019) and Streamline Technologies, (2018).

The basic modeling framework consists of 1D nodes and links to represent overland flow along the river network, a 2D flexible mesh for simulating surface water (SW) flow in rest of the watershed (including the floodplains), a 2D flexible mesh for modeling groundwater (GW) flow and a storage layer between the overland and groundwater meshes representing vadose zone processes. All these elements can interact with each other which allows for a single fully-integrated system of equations. Precipitation received by the overland region is partitioned between the overland region and vadose zone. The water in the overland region is routed through the overland mesh while the water that enters the soil column is stored in the vadose zone. Water from the vadose zone flows into GW from where it can either remain stored in GW, move to the overland region through seepage or return to vadose zone.

The river network is discretized in the form of 1D nodes which are connected by 1D links which transport water from one node to another. The links can be modified to include hydraulic structures such as weirs, culverts or bridges. The 1D river network interacts with the overland flow in the floodplains (and the rest of the watershed) through the 1D-2D interface along the channel boundary (banks). The 2D overland flow is characterized by a triangular mesh of flexible resolution also known as a triangular irregular network (TIN). The modeler ensures that all topographic features relevant to overland flow of water are adequately represented in TIN. Each

988 vertex of the TIN has a honeycomb shaped subbasin which is created by joining the midpoints of
989 the triangle sides to the geometric center of the triangular element in the TIN. These honeycombs
990 are further divided into control volumes (CV) by intersecting them with the geospatial datasets
991 used for parametrization. This ensures that the sub-grid variability in the geospatial datasets within
992 each element of the TIN is conserved. Each CV acts as a subbasin where all hydrologic
993 computations occur. The 2D overland flow occurs along the edges of the TIN. ICPR implements
994 a finite volume discretization for conservation of mass as depicted in Equations A1-A4.

995

996 $$dz = \left(\frac{(Q_{in} - Q_{out})}{A_{surface}}\right) dt \quad \text{(Equation A1)}$$

997 $$Z_{t+dt} = Z_t + dz \quad \text{(Equation A2)}$$

998 $$Q_{in} = \sum Q_{link_{in}} + \sum Q_{runoff} + \sum Q_{external} + \sum Q_{seepage} \quad \text{(Equation A3)}$$

999 $$Q_{out} = \sum Q_{link_{out}} + \sum Q_{irrigation} \quad \text{(Equation A4)}$$

1000

1001 where, dz = incremental change in stage (L); dt= computational time-step (T); Q_{in}= total
1002 inflow rate (L^3T^{-1}); Q_{out}= total outflow rate (L^3T^{-1}); $A_{surface}$ = wet surface area (L^2); Z_{t+dt} =
1003 current water surface elevation (WSE) (L); Z_t = previous WSE (L); $\sum Q_{link_{in}}$= sum of all link
1004 flow rates entering a control volume (L^3T^{-1}); $\sum Q_{link_{out}}$= sum of all link flow rates leaving the
1005 control volume (L^3T^{-1}); $\sum Q_{runoff}$ = sum of catchment area runoff (L^3T^{-1}); $\sum Q_{external}$ = sum of
1006 all inflows from external sources such as streamflow gages (L^3T^{-1}); $\sum Q_{seepage}$= sum of lateral

seepage inflow from groundwater model (L^3T^{-1}); $\sum Q_{irrigation}$ = sum of water pulled out of the system for irrigation (L^3T^{-1}).

The overland flow along the 1D link is governed by the energy equation. The flow along the edges of the 2D TIN is governed by diffusive wave equation. The roughness characterization (Manning's *n*) is governed by an exponential decay function relating Manning's n to surface depth. The relevant equations are given below (Equations A6-A9).

$$Q = \left\{\frac{Z_1 - Z_2}{\Delta x C_f}\right\}^{1/2} \quad \text{(Equation A6)}$$

$$n = n_{shallow} e^{(k)(d)} \quad \text{(Equation A7)}$$

$$k = \frac{ln\left(\frac{n_{deep}}{n_{shallow}}\right)}{d_{max}} \quad \text{(Equation A8)}$$

$$S_{f_{avg}} = \frac{4Q^2}{(K_1 + K_2)^2} \quad \text{(Equation A9)}$$

where Q =flow rate (L^3T^{-1}); Δx =length of channel (L); Z_1, Z_2= WSE at upstream end of link, WSE at downstream end of link, respectively (L); C_f = conveyance factor; n = Manning's roughness at depth *d*; $n_{shallow}$ = Manning's roughness at ground surface; n_{deep} = Manning's roughness at depth = d_{max}; *k* = exponential decay factor; *d* = depth of flow; d_{max} = user specified maximum depth for transitioning to n_{deep}; K_1 *and* K_2 = channel conveyance (L^3T^{-1}) at two cross-sections; and $S_{f_{avg}}$ = average friction slope across two cross-sections.

The vadose zone processes are represented through soil moisture accounting and recharge. ICPR uses a vertical layer method where the vadose zone (region between the ground surface and water table (GWT)) is divided into three vertical layers. Each layer has its own unique soil

1026 characterization which allows ICPR to account for the heterogeneity in soil properties with depth.
1027 Each layer is further subdivided into ten cells (total of 30 cells) to track the movement of water
1028 through the vadose zone. Water enters the vadose zone from the ground surface (infiltration) and
1029 moves in the downward direction through the cells. This movement is governed by the unsaturated
1030 conductivity and moisture content of each cell starting from the top cell to the bottom cell as per
1031 the Brooks-Corey method (Equation A10).

1032 $$\frac{K(\theta)}{K_s} = \left(\frac{\theta-\theta_r}{\varphi-\theta_r}\right)^n \qquad \text{(Equation A10)}$$

1033 where, θ = current moisture content; θ_r = residual moisture content; φ = saturated moisture
1034 content; $K(\theta)$ = unsaturated vertical conductivity at θ; K_s = saturated vertical conductivity; n =
1035 $3 + \frac{2}{\lambda}$; and λ = pore size index.

1036 If the moisture content of the bottom cell exceeds its saturation capacity (saturated moisture
1037 content), the extra flux is delivered to the groundwater and the bottommost cell's moisture content
1038 is set to saturation. Next, a mass balance is performed from the bottommost cell to the topmost cell
1039 to update the moisture content each cell to ensure that the moisture content in the cells do not
1040 exceed saturation capacity. This allows fluxes to move in both direction (surface to GW and GW
1041 to surface) and reflects the drying or wetting of the vadose zone based on the hydraulic fluxes. If
1042 the GWT elevation exceeds the elevation of a cell, that cell is removed from the vadose zone and
1043 becomes a part of the GW. If, on the other hand, the GWT elevation decreases, additional cells
1044 with field capacity may be added to the vadose zone to account for the drying.

1045 The GW is represented as a TIN (2D flexible mesh) similar to the overland 2D flow. GW
1046 is bounded vertically by the vadose zone at the top and a bedrock layer at the bottom. The bedrock

1047 layer is assumed to be impenetrable. The movement in water is represented by a finite element
1048 formulation of the continuity equation depicting 2D unsteady phreatic flow (Equation A11)

1049 $$n\frac{\partial h}{\partial t} = -\frac{\partial (uh)}{\partial x} - \frac{\partial (vh)}{\partial y} \quad \text{(Equation A11)}$$

1050 where, n is the fillable porosity (or specific yield); h is the GW elevation (piezometric
1051 head); u, v are the velocity vector components; t is time; and x, y are the Cartesian coordinates.
1052 The velocity vectors for isotropic media are represented by Equation A12.

1053 $$u = -K.\frac{\partial h}{\partial x}\text{; and, } v = -K.\frac{\partial h}{\partial y} \quad \text{(Equation A12)}$$

1054 where n is the fillable porosity (or specific yield); h is the GW elevation (piezometric head,
1055 L); u, v are the velocity vector components (LT^{-1}); t is time (T). Equation A11 and A12 are solved
1056 simultaneously using Galerkin approximation and Green's Theorem to develop a set of partial
1057 differential equations. The partial differential equations are solved for six nodes of the GW TIN
1058 (three vertices of each triangular element and midpoint of each side of the triangle) using a
1059 quadratic interpolation function shown in Equation A13.

1060 $$h = Ax^2 + By^2 + Cxy + Dx + Ey + F \quad \text{(Equation A13)}$$

1061 where x, y are the Cartesian coordinates (L); K is the permeability (conductivity) of the
1062 porous media; A – F = coefficients of the six-point quadratic function. The set of equation is solved
1063 using the Cholesky method and provides estimates of water transport, storage variation, and
1064 external flows into the vadose zone and overland flow region across the entire GW TIN. Finally,
1065 the seepage rates are calculated using Equation A14.

1066 $$Q_{seepage} = \frac{(h_1 - h_2)\times(A)\times\varphi_b}{dt_{gw}} \quad \text{(Equation A14)}$$

where $Q_{seepage}$ = seepage rate (L^3T^{-1}); h_1= calculated GWT elevation (L); h_2 = ground surface elevation at node (L); A_{gw}= groundwater control volume surface area (L^2); φ_b = below ground fillable porosity; and dt_{gw} = groundwater computational time increment (T).

Reference

Afshari, S., Tavakoly, A.A., Rajib, M.A., Zheng, X., Follum, M.L., Omranian, E., Fekete, B.M., 2018. Comparison of new generation low-complexity flood inundation mapping tools with a hydrodynamic model. J. Hydrol. 556, 539–556. https://doi.org/10.1016/j.jhydrol.2017.11.036

Altenau, E.H., Pavelsky, T.M., Bates, P.D., Neal, J.C., 2017. The effects of spatial resolution and dimensionality on modeling regional-scale hydraulics in a multichannel river. Water Resour. Res. 53, 1683–1701. https://doi.org/10.1002/2016WR019396

Banks, E.W., Simmons, C.T., Love, A.J., Shand, P., 2011. Assessing spatial and temporal connectivity between surface water and groundwater in a regional catchment : Implications for regional scale water quantity and quality. J. Hydrol. 404, 30–49. https://doi.org/10.1016/j.jhydrol.2011.04.017

Baratelli, F., Flipo, N., Moatar, F., 2016. Estimation of stream-aquifer exchanges at regional scale using a distributed model: Sensitivity to in-stream water level fluctuations, riverbed elevation and roughness. J. Hydrol. 542, 686–703. https://doi.org/10.1016/j.jhydrol.2016.09.041

Bhuyian, N.M., Kalyanapu, A.J., Nardi, F., 2015. Approach to Digital Elevation Model Correction by Improving Channel Conveyance. J. Hydrol. Eng. 20, 1–10. https://doi.org/10.1061/(ASCE)HE.1943-5584.0001020.

Brown, R.A., Pasternack, G.B., Wallender, W.W., 2014. Synthetic river valleys: Creating prescribed topography for form-process inquiry and river rehabilitation design. Geomorphology 214, 40–55. https://doi.org/10.1016/j.geomorph.2014.02.025

Brunner, P., Therrien, R., Renard, P., Simmons, C.T., Franssen, H.J.H., 2017. Advances in understanding river-groundwater interactions. Rev. Geophys. 55, 818–854. https://doi.org/10.1002/2017RG000556

Cardenas, M.B., Jiang, X.W., 2010. Groundwater flow, transport, and residence times through topography-driven basins with exponentially decreasing permeability and porosity. Water Resour. Res. https://doi.org/10.1029/2010WR009370

Chow, R., Wu, H., Bennett, J.P., Dugge, J., Wöhling, T., Nowak, W., 2019. Sensitivity of Simulated Hyporheic Exchange to River Bathymetry: The Steinlach River Test Site. Groundwater 57, 378–391. https://doi.org/10.1111/gwat.12816

Cienciala, P., Pasternack, G.B., 2017. Floodplain inundation response to climate, valley form, and flow regulation on a gravel-bed river in a Mediterranean-climate region. Geomorphology 282, 1–17. https://doi.org/10.1016/j.geomorph.2017.01.006

Claxton, A.J., Bates, P.D., Cloke, H.L., 2003. Mixing of Hillslope, River, and Alluvial Ground Waters in Lowland Floodplains. Ground Water 41, 926–936. https://doi.org/10.1111/j.1745-6584.2003.tb02435.x

Cook, A., Merwade, V., 2009. Effect of topographic data , geometric configuration and modeling approach on flood inundation mapping. J. Hydrol. 377, 131–142. https://doi.org/10.1016/j.jhydrol.2009.08.015

Czuba, J.A., David, S.R., Edmonds, D.A., Ward, A.S., 2019. Dynamics of Surface-Water Connectivity in

1108 a Low-Gradient Meandering River Floodplain. Water Resour. Res. 55, 1849–1870.
1109 https://doi.org/10.1029/2018WR023527

1110 Dey, S., 2016. Role of river bathymetry in hydraulic modeling of river channels. Open Access Theses.
1111 Purdue University.

1112 Dey, S., Saksena, S., Merwade, V., 2019. Assessing the effect of different bathymetric models on
1113 hydraulic simulation of rivers in data sparse regions. J. Hydrol. 575, 838–851.
1114 https://doi.org/10.1016/j.jhydrol.2019.05.085

1115 Doble, R., Brunner, P., McCallum, J., Cook, P.G., 2012. An Analysis of River Bank Slope and
1116 Unsaturated Flow Effects on Bank Storage. Ground Water 50, 77–86.
1117 https://doi.org/10.1111/j.1745-6584.2011.00821.x

1118 Fleckenstein, J.H., Krause, S., Hannah, D.M., Boano, F., 2010. Groundwater-surface water interactions:
1119 New methods and models to improve understanding of processes and dynamics. Adv. Water Resour.
1120 33, 1291–1295. https://doi.org/10.1016/j.advwatres.2010.09.011

1121 Flipo, N., Mouhri, A., Labarthe, B., Biancamaria, S., Rivière, A., Weill, P., 2014. Continental
1122 hydrosystem modelling: the concept of nested stream-aquifer interfaces. Hydrol. Earth Syst. Sci. 18,
1123 3121–3149. https://doi.org/10.5194/hess-18-3121-2014

1124 Follum, M.L., Vera, R., Tavakoly, A.A., Gutenson, J.L., 2020. Improved accuracy and efficiency of flood
1125 inundation mapping of low-, medium-, and high-flow events using the AutoRoute model. Nat.
1126 Hazards Earth Syst. Sci. 20, 625–641. https://doi.org/10.5194/nhess-20-625-2020

1127 Gichamo, T.Z., Popescu, I., Jonoski, A., Solomatine, D., 2012. River cross-section extraction from the
1128 ASTER global DEM for flood modeling. Environ. Model. Softw. 31, 37–46.
1129 https://doi.org/10.1016/j.envsoft.2011.12.003

1130 Glenn, J., Tonina, D., Morehead, M.D., Fiedler, F., Benjankar, R., 2016. Effect of transect location,
1131 transect spacing and interpolation methods on river bathymetry accuracy. Earth Surf. Process.
1132 Landforms 41, 1185–1198. https://doi.org/10.1002/esp.3891

1133 Grimaldi, S., Li, Y., Walker, J.P., Pauwels, V.R.N., 2018. Effective Representation of River Geometry in
1134 Hydraulic Flood Forecast Models. Water Resour. Res. https://doi.org/10.1002/2017WR021765

1135 Grimaldi, S., Schumann, G.J.P., Shokri, A., Walker, J.P., Pauwels, V.R.N., 2019. Challenges,
1136 Opportunities, and Pitfalls for Global Coupled Hydrologic-Hydraulic Modeling of Floods. Water
1137 Resour. Res. 55, 5277–5300. https://doi.org/10.1029/2018WR024289

1138 Jung, M., Burt, T.P., Bates, P.D., 2004. Toward a conceptual model of floodplain water table response.
1139 Water Resour. Res. 40, 1–13. https://doi.org/10.1029/2003WR002619

1140 Käser, D., Graf, T., Cochand, F., Mclaren, R., Therrien, R., Brunner, P., 2014. Channel Representation in
1141 Physically Based Models Coupling Groundwater and Surface Water: Pitfalls and How to Avoid
1142 Them. Groundwater 52, 827–836. https://doi.org/10.1111/gwat.12143

1143 Kollet, S.J., Maxwell, R.M., 2008. Capturing the influence of groundwater dynamics on land surface
1144 processes using an integrated, distributed watershed model. Water Resour. Res.
1145 https://doi.org/10.1029/2007WR006004

1146 Legleiter, C.J., Kyriakidis, P.C., McDonald, R.R., Nelson, J.M., 2011. Effects of uncertain topographic
1147 input data on two-dimensional flow modeling in a gravel-bed river. Water Resour. Res. 47, 1–24.
1148 https://doi.org/10.1029/2010WR009618

1149 Mejia, A.I., Reed, S.M., 2011. Evaluating the effects of parameterized cross section shapes and simplified
1150 routing with a coupled distributed hydrologic and hydraulic model. J. Hydrol. 409, 512–524.
1151 https://doi.org/10.1016/j.jhydrol.2011.08.050

1152 Merwade, V., 2004. Geospatial Description of River Channels in Three Dimensions. The University of
1153 Texas at Austin.

1154 Merwade, V.M., 2004. A GIS framework for describing river channel bathymetry. University of Texas at
1155 Austin.

1156 Merwade, V.M., Maidment, D.R., Goff, J.A., 2006. Anisotropic considerations while interpolating river
1157 channel bathymetry. J. Hydrol. 331, 731–741. https://doi.org/10.1016/j.jhydrol.2006.06.018

1158 Nash, J.E., Sutcliffe, J. V, 1970. River Flow Forecasting Through Conceptual Models Part I-A Discussion
1159 of Principles. J. Hydrol. 10, 282–290. https://doi.org/10.1016/0022-1694(70)90255-6

1160 Neal, J.C., Odoni, N.A., Trigg, M.A., Freer, J.E., Garcia-Pintado, J., Mason, D.C., Wood, M., Bates, P.D.,
1161 2015. Efficient incorporation of channel cross-section geometry uncertainty into regional and global
1162 scale flood inundation models. J. Hydrol. 529, 169–183.
1163 https://doi.org/10.1016/j.jhydrol.2015.07.026

1164 Osman, Y.Z., Bruen, M.P., 2002. Modelling stream–aquifer seepage in an alluvial aquifer: an improved
1165 loosing-stream package for MODFLOW. J. Hydrol. 264, 69–86. https://doi.org/10.1016/S0022-
1166 1694(02)00067-7

1167 Price, R.K., 2009. An optimized routing model for flood forecasting. Water Resour. Res. 45, 1–15.
1168 https://doi.org/10.1029/2008WR007103

1169 Rajib, A., Liu, Z., Merwade, V., Tavakoly, A.A., Follum, M.L., 2020. Towards a large-scale locally
1170 relevant flood inundation modeling framework using SWAT and LISFLOOD-FP. J. Hydrol. 581,
1171 124406. https://doi.org/10.1016/j.jhydrol.2019.124406

1172 Rodríguez, E., Durand, M., Frasson, R.P. de M., 2020. Observing Rivers With Varying Spatial Scales.
1173 Water Resour. Res. 56. https://doi.org/10.1029/2019WR026476

1174 Saksena, S., Dey, S., Merwade, V., Singhofen, P.J., 2020. A Computationally Efficient and Physically
1175 Based Approach for Urban Flood Modeling Using a Flexible Spatiotemporal Structure. Water
1176 Resour. Res. 56. https://doi.org/10.1029/2019WR025769

1177 Saksena, S., Merwade, V., 2017a. Integrated Modeling of Surface-Subsurface Processes to Understand
1178 River-Floodplain Hydrodynamics in the Upper Wabash River Basin, in: World Environmental and
1179 Water Resources Congress 2017. American Society of Civil Engineers, Reston, VA, pp. 60–68.
1180 https://doi.org/10.1061/9780784480595.006

1181 Saksena, S., Merwade, V., 2017b. Deterministic Approach to Identify Ordinary High Water Marks Using
1182 Hydrologic and Hydraulic Attributes. J. Irrig. Drain. Eng. 143.
1183 https://doi.org/10.1061/(ASCE)IR.1943-4774.0001148.

1184 Saksena, S., Merwade, V., 2015. Incorporating the effect of DEM resolution and accuracy for improved
1185 flood inundation mapping. J. Hydrol. 530, 180–194. https://doi.org/10.1016/j.jhydrol.2015.09.069

1186 Saksena, S., Merwade, V., Singhofen, P.J., 2021. An Alternative Approach for Improving Prediction of
1187 Integrated Hydrologic-Hydraulic Models by Assessing the Impact of Intrinsic Spatial Scales Water
1188 Resources Research. Water Resour. Res. 57, 1–31. https://doi.org/10.1029/2020WR027702

1189 Saksena, S., Merwade, V., Singhofen, P.J., 2019. Flood inundation modeling and mapping by integrating
1190 surface and subsurface hydrology with river hydrodynamics. J. Hydrol. 575, 1155–1177.
1191 https://doi.org/10.1016/j.jhydrol.2019.06.024

1192 Saleh, F., Ducharne, A., Flipo, N., Oudin, L., Ledoux, E., 2012. Impact of river bed morphology on
1193 discharge and water levels simulated by a 1D Saint – Venant hydraulic model at regional scale. J.
1194 Hydrol. 476, 1–9. https://doi.org/10.1016/j.jhydrol.2012.10.027

1195 Schaperow, J.R., Li, D., Margulis, S.A., Lettenmaier, D.P., 2019. A Curve-Fitting Method for Estimating
1196 Bathymetry From Water Surface Height and Width. Water Resour. Res. 55, 4288–4303.
1197 https://doi.org/10.1029/2019WR024938

1198 Stewart, M.D., Bates, P.D., Anderson, M.G., Price, D.A., Burt, T.P., 1999. Modelling floods in
1199 hydrologically complex lowland river reaches. J. Hydrol. 223, 85–106.
1200 https://doi.org/10.1016/S0022-1694(99)00112-2

1201 Tijerina, D., Condon, L., FitzGerald, K., Dugger, A., O'Neill, M.M., Sampson, K., Gochis, D., Maxwell,
1202 R., 2021. Continental Hydrologic Intercomparison Project, Phase 1: A Large-Scale Hydrologic
1203 Model Comparison Over the Continental United States. Water Resour. Res. 57, 1–27.
1204 https://doi.org/10.1029/2020WR028931

1205 Tran, Q.Q., Meert, P., Huysmans, M., Willems, P., 2020. On the importance of river hydrodynamics in
1206 simulating groundwater levels and baseflows. Hydrol. Process. hyp.13667.
1207 https://doi.org/10.1002/hyp.13667

1208 Trigg, M.A., Wilson, M.D., Bates, P.D., Horritt, M.S., Alsdorf, D.E., Forsberg, B.R., Vega, M.C., 2009.
1209 Amazon flood wave hydraulics. J. Hydrol. 374, 92–105.
1210 https://doi.org/10.1016/j.jhydrol.2009.06.004

1211 Vergnes, J.-P., Habets, F., 2018. Impact of river water levels on the simulation of stream–aquifer
1212 exchanges over the Upper Rhine alluvial aquifer (France/Germany). Hydrogeol. J. 26, 2443–2457.
1213 https://doi.org/10.1007/s10040-018-1788-0

1214 Wing, O.E.J., Bates, P.D., Sampson, C.C., Smith, A.M., Johnson, K.A., Erickson, T.A., 2017. Validation
1215 of a 30 m resolution flood hazard model of the conterminous United States. Water Resour. Res. 53,
1216 7968–7986. https://doi.org/10.1002/2017WR020917

1217 Wörman, A., Packman, A.I., Marklund, L., Harvey, J.W., Stone, S.H., 2006. Exact three-dimensional
1218 spectral solution to surface-groundwater interactions with arbitrary surface topography. Geophys.
1219 Res. Lett. 33, L07402. https://doi.org/10.1029/2006GL025747

1220 Yoon, Y., Durand, M., Merry, C.J., Clark, E.A., Andreadis, K.M., Alsdorf, D.E., 2012. Estimating river
1221 bathymetry from data assimilation of synthetic SWOT measurements. J. Hydrol. 464–465, 363–375.
1222 https://doi.org/10.1016/j.jhydrol.2012.07.028

1223